International Journal of Biological Macromolecules 364 (2026) 152317

Contents lists available at ScienceDirect

International Journal of Biological Macromolecules

journal homepage: www.elsevier.com/locate/ijbiomac

Modulating STAT3 pathway in breast cancer: Improved activity of T40214 aptamer by peptide-based nanofibers delivering

Rosa Bellavita [a,1], Daniela Benigno [a,1], Marialuisa Piccolo [a,1], Simone Braccia [a], Carla Aliberti [a], Federica Iazzetti [a], Antonella Virgilio [a], Veronica Esposito [a], Federica Donadio [b], Emanuela Esposito [b], Antonio Giordano [c,d], Annarita Falanga [e], Carlo Irace [a], Aldo Galeone [a,*], Stefania Galdiero [a,*]

[a] Department of Pharmacy, University of Naples Federico II, Napoli, 80131, Italy
[b] Institute of Applied Sciences and Intelligent Systems (ISASI), Naples Cryo Electron Microscopy Laboratory – EYE LAB, National Research Council (CNR), Via Pietro Castellino 111, 80131, Napoli, Italy
[c] Sbarro Institute for Cancer Research and Molecular Medicine and Center of Biotechnology, College of Science and Technology, Temple University, 1900 N 12 St, Philadelphia, PA 19122, USA
[d] Department of Life, Health and Environmental Sciences, University of L'Aquila, L'Aquila, Italy
[e] Department of Agricultural Sciences, University of Naples Federico II, Via Università 100, Portici, 80055, Italy

ARTICLE INFO

Keywords:
Self-assembled peptides
Nanofiber
Aptamer
Delivery
Breast cancer

ABSTRACT

G-quadruplex (G4)-forming aptamers are highly selective oligonucleotides with significant potential in cancer therapy, acting as inhibitors of oncogenic proteins such as Signal Transducer and Activator of Transcription 3 (STAT3). Among them, the G4-forming aptamer T40214 (STAT) effectively modulates STAT3 signaling; however, its clinical translation is currently hindered by poor cellular internalization. In this study, we developed a multifunctional peptide amphiphile (PA)-based nanofiber (NF) to enhance the intracellular delivery and tumor selectivity of the G4 STAT aptamer in breast cancer cells. The nanofiber integrates a poly-arginine domain for aptamer binding, the cell-penetrating peptide gH625 to promote internalization, and the EGFR-targeting peptide P22 for selective tumor cell recognition. The aptamer-decorated NFs exhibited an average fiber length of 100 ± 30 nm and a diameter of 25 ± 5 nm and remained stable under physiological conditions. Aptamer binding was confirmed by agarose gel electrophoresis and circular dichroism. The resulting STAT-NF complex showed stability over time and varying temperature and ionic strength effects. A markedly enhanced antiproliferative activity of the STAT was observed in multiple triple-negative breast cell models, proved by an efficient and selective uptake in a triple negative breast cancer cell line. Mechanistic studies revealed that STAT-NF internalization occurs predominantly through an endocytosis-independent translocation mechanism, and the activation of apoptotic pathways by the released STAT was confirmed. These results highlight PA-based nanofibers as an effective and versatile platform for tumor-targeted delivery of G4 aptamers.

1. Introduction

G-quadruplex (G4)-forming aptamers constitute a distinctive class of oligonucleotides capable of adopting four-stranded architectures stabilized by Hoogsteen hydrogen bonds between guanine residues [1–3]. Their intrinsic ability to selectively recognize specific protein targets under physiological conditions, together with their low immunogenicity, broad chemical tunability [4], and the feasibility of introducing precise site-directed modifications, has established G4 aptamers as highly promising candidates for a wide range of biomedical applications, with particular relevance in oncology [5–8].

Several G4-based sequences have been engineered to inhibit key oncogenic proteins, such as nucleolin [9], Vascular Endothelial Growth Factor (VEGF) [10], and Signal Transducer and Activator of Transcription-3 (STAT3) [11], thereby modulating signaling pathways that drive tumor proliferation, survival, and metastatic progression.

* Corresponding authors at: Department of Pharmacy, University of Naples Federico II, Napoli, Italy.
E-mail addresses: galeone@unina.it (A. Galeone), sgaldier@unina.it (S. Galdiero).
[1] Rosa Bellavita, Daniela Benigno and Marialuisa Piccolo contributed equally to this work.

https://doi.org/10.1016/j.ijbiomac.2026.152317
Received 22 January 2026; Received in revised form 27 April 2026; Accepted 28 April 2026
Available online 29 April 2026

Among these targets, STAT3 emerges as a pivotal regulator of cellular homeostasis and a major driver of pathological processes, with a particularly strong association with cancer [12,13]. Under physiological conditions, STAT3 resides in the cytoplasm in an inactive form. Upon stimulation by cytokines such as IL-6 or other extracellular ligands [14], phosphorylation at the C-terminal domain induces homo- or heterodimerization, enabling nuclear translocation and subsequent binding to specific DNA response elements [15,16]. This process initiates the transcription of genes essential for cell survival, proliferation, inflammation, and angiogenesis [17]. Aberrant STAT3 signaling is critically involved in oncogenesis and tumor progression [18], primarily through the transcriptional upregulation of anti-apoptotic proteins, cell-cycle mediators, and pro-angiogenic factors [19]. Persistent STAT3 activation has been reported in multiple malignancies, including prostate, head and neck, lung, and breast cancers [20–22], highlighting its widespread relevance in malignant transformation and its attractiveness as a therapeutic target [23].

Given its multifaceted role in tumor biology, a variety of structurally diverse compounds have been developed to inhibit STAT3 by interfering with different steps of its activation cascade [24–27].

Within this context, G4-aptamers have emerged as a particularly attractive class of STAT3 protein inhibitors. Among these, the G4-forming aptamer T40214 (STAT), with sequence $(G_3C)_4$, structurally adopts a dimeric 5′–5′ end-stacked G4 arrangement, in which each parallel monomer contains three all-*anti* G-tetrads and three single-cytidine propeller loops [11,28,29]. Functionally, the aptamer STAT acts by suppressing IL-6-induced STAT3 activation and downregulating STAT3-dependent gene expression in cancer cells [11]. These effects lead to enhanced apoptosis and reduced proliferation in prostate and breast cancer models [22,30], along with significant antitumor activity in xenograft models [31].

Despite these encouraging advances, several challenges still limit the clinical translation of G-quadruplex aptamers [32]. Their intrinsically low cytotoxicity often results in modest antiproliferative activity, and their stability in biological environments is hampered by rapid degradation by serum nucleases, fast renal clearance, and overall unfavorable pharmacokinetic profiles [33,34]. Furthermore, their highly negatively charged nature restricts cellular internalization, which typically relies on endocytic pathways and consequently limits intracellular accumulation [35,36]. These factors collectively underscore the need for advanced delivery strategies that can enhance intracellular uptake and ensure efficient engagement of intracellular targets [35,37–39]. In this context, nanotechnology-based delivery systems offer a promising approach to improve the therapeutic potential of G4 aptamers by enabling targeted, efficient delivery to tumor cells [40–44].

Both organic and inorganic nanoparticles are widely explored as carriers for anticancer therapeutics [45–47]; however, the inherent toxicity associated with most inorganic materials and their low ability to overcome endosomal entrapment significantly limit their translational applicability [48]. In contrast, biocompatible and biodegradable materials provide an advantageous platform for controlled and targeted delivery, as they break down into small molecules that can be readily cleared from the body [49]. Within this category, peptide amphiphiles (PAs) represent a fascinating class of building blocks [50]. By modulating the hydrophobic-hydrophilic balance, PAs spontaneously self-assemble into stable, structurally defined nanofibers with customizable surfaces [51]. This enables the creation of versatile nanoplatforms tailored for targeted therapeutic applications. Their modular design also allows precise tuning of bioactivity through the type and density of surface moieties, without compromising the integrity of the underlying nanostructure. Nanoparticle shape is another critical parameter influencing the efficiency of our targeted delivery system [52]. In contrast to spherical nanosystems commonly employed for aptamer delivery, nonspherical systems such as nanofibers enhance cellular uptake and provide increased surface area for multi-functionalization [53]. In line with this, we previously demonstrated that our PA-based nanofibers can effectively carry multiple drugs targeting triple-negative breast cancer or glioblastoma, enhancing cellular internalization and permitting dose reduction while maintaining therapeutic efficacy [54–56]. Furthermore, an additional key advantage of these nanofibers is their ability to enter cells while only partially relying on endocytic pathways. This behavior helps them avoid endosomal entrapment, enabling the direct release of the drug into the cytoplasm. This property is conferred by the presence of the peptide gH625 on their surface, a peptide developed in our laboratory and extensively validated for its internalization mechanism [54,55].

In this study, we employed our PA-based nanofiber vector (Fig. 1) to enhance the cellular internalization of the G4 STAT and promote its selective delivery to breast cancer cells, thereby enabling effective STAT3 targeting and reduced tumor cell proliferation. Nanofiber internalization is facilitated by functionalization with the cell-penetrating peptide gH625 [57,58]. Tumor-specific targeting was achieved by decorating the nanofiber surface with the EGFR-binding peptide P22, enabling selective delivery to breast cancer cells overexpressing Epidermal Growth Factor Receptor (EGFR) [59]. The aptamer loading onto the nanofiber surface was achieved through non-covalent electrostatic interactions mediated by a poly-arginine sequence whose intrinsic cationicity facilitates strong interactions with the negatively charged phosphate backbone of the G4 aptamer [60].

Herein, we described the design and formation of the aptamer-decorated nanofiber and its characterization in terms of size, morphology, and surface charge. The binding between the nanofiber and aptamer was assessed by agarose gel electrophoresis, circular dichroism, and fluorescence spectroscopy, while the stability of the resulting complex was evaluated under different experimental conditions. Moreover, the delivery efficiency of STAT was assessed across several breast cancer cell lines, demonstrating selective uptake by tumor cells and a consequently markedly enhanced antiproliferative activity. The internalization mechanism was elucidated by fluorescence microscopy, and the activation of apoptotic pathways by delivered STAT was studied.

In conclusion, our results showed that the nanofiber represents an effective platform for aptamer delivery, capable of enhancing their biological function by promoting an efficient and tumor-targeted cellular internalization. Our findings highlight the potential of this nanofiber to serve as a versatile delivery vehicle capable of being tailored for a wide range of nucleic acid-based therapeutics.

2. Materials and methods

2.1. Reagents and cell lines

2.1.1. Chemical reagents

The canonical N^{α}-Fmoc amino acids were purchased from GL Biochem Ltd. (Shanghai, China). The unnatural amino acid Fmoc-L-Lys (Mtt)-OH, the Rink amide p-methylbenzhydrylamine (MBHA) resin, piperidine, trifluoroacetic acid (TFA), and the coupling reagents HATU (1-[bis(dimethylamino)methylene]-1H-1,2,3-triazolo[4,5-b]pyridinium 3-oxid hexafluorophosphate), pure oxyma, and *N,N′*-diisopropylcarbodiimide (DIC), were purchased from Iris-Biotec GmbH (Marktredwitz, Germany). Nile Red, Thioflavin T, *N,N*-diisopropylethylamine (DIEA), triisopropylsilane (TIS), agarose, and sodium chloride were acquired from Merck (Milan, Italy). 6-FAM Glyceryl Support 500Å was purchased from ChemGenes (Wilmington, United States), while 3′-phosphoramidites were acquired from LGC Biosearch Technologies (Glasgow, UK).

2.1.2. Cell lines

All cell lines used in this study were acquired from the ATCC cellular bank. These included epithelial-like type human breast adenocarcinoma cells, i.e. MDA-MB-231 (HTB-26 ™), MCF-7 (HTB-22 ™) and T47D (HTB-133 ™). In addition, Primary Human Dermal Fibroblasts (HDFa)

(PCS-201-012 ™) were used as healthy control cells.

2.2. Aptamer synthesis

STAT and STAT-FAM aptamers were synthesized by K&A H-16 DNA synthesizer (K&A Labs GmBH, Schaafheim, Germany) using solid-phase β-cyanoethyl phosphoramidite chemistry at 5 μmol scale [11]. The synthesis was carried out using normal 3′-phosphoramidites. For STAT-FAM ODN, a 3'-(6-Fluorescein) CPG support has been used to add the fluorescein label at the 3'-terminus. The detachment from the support and the deprotection of the oligomers were carried out by treatment with concentrated aqueous ammonia at 55 °C overnight. The combined filtrates and washings were concentrated under reduced pressure, redissolved in H_2O, analyzed, and purified by high-performance liquid chromatography on a Nucleogel SAX column (Macherey-Nagel, Duren, Germany, 1000-8/46) using buffer A (20 mM NaH_2PO_4/Na_2HPO_4 aqueous solution (pH 7.0) containing 20% (v/v) CH_3CN) and buffer B (1 M NaCl, 20 mM NaH_2PO4/Na_2HPO_4 aqueous solution (pH 7.0) containing 20% (v/v) CH_3CN); a linear gradient from 0% to 100% B for 45 min and a flow rate of 1 mL/min were used. The fractions of the oligomers were collected and successively desalted by Sep-pak cartridges (C-18). The isolated oligomers proved to be >98% pure by HPLC (Fig. S1-S2). Samples were prepared at an ODN concentration of 200 μM using a potassium phosphate buffer (10 mM KH_2PO_4/K_2HPO_4, 70 mM KCl, pH 7.0) and submitted to the annealing procedure (heating at 90 °C and slowly cooling at room temperature). The resulting solutions were used as stock solutions for all subsequent experiments.

2.3. Peptide synthesis for nanofiber construction

For the nanofiber fabrication, all peptides P1–P3, P6, and P7 (Table 1), were obtained by applying the solid-phase peptide synthesis (SPPS) combined with the ultrasound (US) strategy [61–63]. All peptides were constructed on the Rink-amide resin as solid support to have the amidated C-terminus.

Fmoc-Lys(Mtt)-OH was introduced as the first amino acid to allow subsequent attachment of the nonadecanoic acid (C19) to its side chain after the Mtt deprotection. This residue, as well as all amino acids, was coupled by preforming double-coupling strategy under US irradiation: *1st cycle:* DIC (2 equiv), Oxyma (2 equiv) in DMF for 10 min; *2nd cycle*: HATU (2 equiv), and DIPEA (4 equiv) in DMF for 10 min. Whereas, Fmoc deprotection was carried out with a solution of 20 % piperidine in DMF by two 5 min-cycles. After the peptide elongation, the Mtt group was removed by treating the resin with a cocktail of TFA/TIS/DCM (1:5:94, *v:v:v*) for 15 times, and the complete removal was ascertained both by colorimetric Kaiser test and High-performance liquid chromatography (HPLC) analysis. Then, the C19 tail was coupled by HATU (2 equiv) and DIPEA (4 equiv) in NMP for 2 h under conventional stirring; the coupling was repeated twice. Before peptide cleavage, consisting of treating the resin with the strong acid mixture TFA:TIS:H_2O (95:2.5:2.5, *v:v:v*), each peptide identity was verified by Electrospray Ionization Mass Spectrometry (ESI-MS) analysis. Moreover, for the purification, each crude peptide was dissolved in a mixture of 10 % 1,1,1,3,3,3-Hexafluoro-2-propanol (HFIP) in H_2O containing 0.1 % TFA, and purified on a Phenomenex Kinetex C18 column (5 μm, 100 Å, 150 × 21.2 mm) using a linear gradient of acetonitrile (0.1 % TFA) in water (0.1 % TFA), from 10 to 90 % over 35 min, with a flow rate of 15 mL/min and UV detection at 220 nm. The pure profile of each peptide was ascertained by the analytical HPLC (Jasco LC-NetII/ADC) by using Phenomenex Jupiter 4u Proteo column (90 Å, 150 × 4.6 mm) (Fig. S3–S7), and their identity was confirmed by ESI-MS analysis (Fig. S8–S12).

Table 1
Peptide sequences for the preparation of nanofiber formulations

Peptide	Sequence
P1	NH_2-GDDS-AAAAAA-K(C19)-$CONH_2$
P2	NH_2-GKRS-AAAAAA-K(C19)-$CONH_2$
P3	NH_2- **HGLASTLTRWAHYNALIRAF**-GKRS-AAAAAA-K(C19)-$CONH_2$
P6	NH_2- **YHWYGYTPENVI**-GKRS-AAAAAA-K(C19)-$CONH_2$
P7	NH_2-**RRRRRR**-Ahx-AAAAAA-K(C19)-$CONH_2$

2.4. Nanofiber physicochemical characterization

2.4.1. Determination of critical aggregation concentration

The critical aggregation concentration (CAC) of self-assembled peptides at the specific ratio in solution was measured using the solvatochromic fluorescent probe Nile Red [64,65]. Each stock peptide solution was prepared in the organic solvent HFIP to favor its monomeric state. We calculated the CAC value of two nanofiber formulations containing different amounts of the poly-arginine peptide P7 (10% and 20%) binding the aptamer T40214. Specifically, we co-assembled the peptides P1:P2:P3:P6:P7 at the ratios of 50:32.5:5:2.5:10 (mol/mol) and 50:22.5:5:2.5:20 (mol/mol), to have NF-P7 (10%) and NF-P7 (20%), respectively. To determine the CAC value, these nanofibers were prepared at concentrations of 0.5, 0.8, 1, 3, 5, 7, 10, 15, 20, 25, 30, and 50 μM. Then, HFIP was evaporated under a nitrogen stream, water (500 μL) was added, and the samples were lyophilized. Each nanofiber sample was hydrated with Nile Red solution (500 nM) for 1 h. Fluorescence spectra were recorded using an excitation wavelength of 550 nm and an emission range of 570–700 nm. CAC values were obtained by plotting the wavelength at maximum fluorescence intensity as a function of peptide concentration and fitting the data using the sigmoidal Boltzmann equation:

$$y = \frac{A1 + A2}{1 + e^{\left(x - \frac{x0}{\Delta x}\right)}} + A2$$

In this equation, the parameters A1 and A2 indicate the upper and lower limits of the sigmoid, respectively, whereas x0 and Δx are the inflection point and steepness of the sigmoid function, respectively.

2.4.2. Morphological characterization

The size and morphology of peptide nanostructures were investigated by Scanning Electron Microscopy (SEM) analysis. A drop of 3 μL of NF suspension was deposited onto a cleaned silicon wafer covered by a gold layer and allowed air-dry at room temperature.

SEM images were acquired using a Thermo Scientific Aquilos 2 Cryo-FIB/SEM dual-beam system (Thermo Fisher Scientific, Waltham, MA, USA). The analysis was performed under carefully controlled conditions to ensure high-resolution surface characterization. Specifically, a beam current of 25 pA and an accelerating voltage of 3 kV were used, the working distance was set to 4.4 mm, and imaging was carried out with the T2 detector, optimized for high-contrast secondary electron collection. All acquisitions were performed at a stage tilt of 0°and magnifications of 50,000x and 65,000x.

2.4.3. Nanofiber stability

The secondary structure of the nanostructure NF-P7 (20%) was determined by performing the circular dichroism (CD) analysis. The nanofiber was prepared at a concentration of 50 μM, and the CD spectrum was recorded from 260 to 190 nm on a Jasco J-1500 CD Spectrometer with a quartz cell (1 cm) at room temperature. Additionally, the nanofiber stability under dilution effect (50, 40, 30 and 20 μM), different ionic strength (from 1 mM to 10 mM NaCl), and pH environments (pH 7 and 5) were also evaluated by CD spectroscopy. All CD spectra were obtained by averaging three scans and converting the signal to molar ellipticity.

2.5. Physicochemical characterization of STAT-NF complex

2.5.1. Agarose gel electrophoresis for STAT and nanofiber binding

The binding between STAT and nanofibers was evaluated by agarose gel electrophoresis. STAT annealed as described above, was prepared at 2 μM in K^+ buffer and incubated with the nanofibers NF-P7 (10%) and NF-P7 (20%) at the STAT:NF molar ratios of 1:5, 1:10, 1:15, 1:20, 1:30, for 25 min at room temperature. Then, each complex was subjected to electrophoresis in Tris-acetate-EDTA (TAE) buffer for 45 min at 90 V/35 mA within a 3 % agarose gel containing GelRed stain (Merck, Milan). The gel visualization occurred under UV light, followed by capturing a digital image of the stained gel using the ChemiDoc Imaging System.

2.5.2. STAT-NF binding by fluorescence assays

The interaction between STAT and the nanofiber was evaluated by fluorescence spectroscopy, using an excitation wavelength of 260 nm for the aptamer. The STAT:NF complexes were prepared at the ratios of 1:5, 1:10, 1:20, 1:30 in K^+ buffer and incubated for 25 min. Each fluorescence spectrum was recorded from 350 to 500 nm. Additionally, the presence of G4 structure, before and after the nanofiber interaction, was assessed by performing the Thioflavin T (ThT) assay. ThT was added at a concentration of 25 μM at the nanofiber alone, STAT alone, and STAT:NF complex at the ratio 1:20. Each ThT spectrum was recorded using an excitation wavelength of 425 nm and an emission range of 470–550 nm.

2.5.3. Zeta potential measurements

The zeta potentials were determined using dynamic light scattering Zetasizer Nano-ZS (Malvern Instruments, Worcestershire, UK) with a He–Ne laser 4 mW operating at 633 nm at a scattering angle fixed at 173° and at 25 °C. The measurements were carried out for nanofiber alone, STAT alone, and the STAT:NF complexes at the ratios of 1:5, 1:10, 1:20, and 1:30 in K^+ buffer. N Zeta potential is reported as the mean value ± S.D. from three measurements.

2.5.4. STAT-NF complex stability

STAT was evaluated for its structural stability under different conditions by CD spectroscopy. The aptamer was prepared at a final concentration of 2 μM in K^+ buffer, and its stability at ionic strength by varying the NaCl concentration from 1 mM to 10 mM and temperature (37, 45, and 60 °C) was investigated.

The binding of the aptamer to NF was analyzed by CD spectroscopy at different molar ratios (1:5, 1:10, 1:15, 1:20, and 1:30) at pH 7 and 25°C. The stability of the STAT:NF complex at 1:20 ratio was subsequently examined under various conditions, including temperature (37, 45, and 60 °C), ionic strength (1-10 mM NaCl), and over time (2, 4, 6, and 24 h).

All CD spectra were recorded on a Jasco J-750 spectropolarimeter using a 1.0 cm path length quartz cuvette, over a wavelength range of 200-320 nm. Each spectrum represents the average of three scans, and the data were converted to molar ellipticity (θ, $deg \cdot cm^2 \cdot dmol^{-1}$).

2.6. Nanofiber preparation for biological studies

The NF P1:P2:P3:P6:P7 (50:22.5:5:2.5:20) was pre-formed at a concentration of 100 μM in water and then complexed with aptamer 5 μM in K^+ buffer at the ratio 1:20. The resulting complex was then diluted to test aptamer concentrations of 2.5, 2, 1, and 0.5 μM.

2.7. Cell cultures

Human breast adenocarcinoma cells, epithelial-like type as MCF-7 (ER+) and MDA-MB-231 (TNBC) cell lines were grown in DMEM (Invitrogen, Paisley, UK) supplemented with 10% fetal bovine serum (FBS, ATCC 30-2020), L-glutamine (2mM, Sigma, Milan, Italy), penicillin (100 units/ml, Sigma) and streptomycin (100 μg/ml, Sigma). Additionally, the human breast epithelial carcinoma T47D (ER+) cell line was cultivated in RPMI-1640 medium. To make the complete growth medium, human recombinant insulin (Gibco #12585-014) (0.5 %) and fetal bovine serum (FBS, ATCC 30-2020) to a final concentration of 10%, were freshly added to the medium prior to use. Primary Human Dermal Fibroblasts (HDFa), used as a healthy cell line, were cultured in Fibroblast Basal Medium supplemented with Fibroblast Growth Kit–Low Serum.

All cell lines were cultured in a humidified 5% CO_2 at 37 °C, according to ATCC recommendations.

2.8. Bioscreens in vitro

In vitro cellular response experiments were assessed using both healthy and cancer human cell lines, cultured in poly-D-lysine–coated 96-well culture plates. Cells were seeded at a density of 10^4/well and allowed to growth for 24 h. Cell cultures were then exposed to STAT, STAT-NF, and the unloaded NF, for 48 and 72 h, using a range of micromolar concentrations (0.5, 1, 2 and 2,5 μM of STAT, *i.e.* 10, 20, 40 and 50 μM of NF), to assess concentration-dependent effects.

Following treatments, two viability assays were performed, which together allowed us to assess a "cell survival index", as previously reported by us [66]. Specifically, this combined approach links cellular responses from two *in vitro* tests: i) MTT assay and ii) cell count.

i) The indirect sign of viability, proliferation, and overall metabolic status of cells was assessed through the colorimetric tetrazolium-based metabolic assay. At the end of MTT incubation period, absorbances of samples' formazan were recorded by using the microplate spectrophotometer (iMark microplate reader, Bio-Rad, Milan, Italy) at a wavelength of 550 nm.
ii) Quantification of cell number was performed using a TC20 automated cell counter (Bio-Rad, Milan, Italy), which ensures reliable total cell counts and live/dead discrimination via trypan blue exclusion.

Data are presented as percentages relative to untreated controls and reported as mean of 3 independent experiments ± SEM (n = 12), analyzed using a curve-fitting software package (GraphPad Prism 8.0).

2.9. Fluorescence-based cellular uptake assay in EGFR-High and EGFR-Low cell lines

Profiling of cellular uptake of STAT-NF was carried out by fluorescent microscopy in breast cancer cell lines characterized by differential EGFR expression. Specifically, MDA-MB-231 cells, which display high levels of EGFR, and MCF-7 cells, exhibiting low receptor expression, were seeded (5×10^4 cells) onto glass coverslips placed in 12-well plates and allowed to adhere for 24 h. After medium replacement, cells were incubated with FITC-labeled STAT-NF for 2 h, corresponding to the predefined time point selected to monitor internalization. At the end of the incubation period, cells were washed three times with PBS, fixed with 4% paraformaldehyde for 10 min at room temperature, and washed again with PBS. Nuclei were counterstained with DAPI, and samples were immediately imaged using a Leica Mica fluorescence microscope. Images were acquired at 10× magnification, maintaining identical exposure settings across all samples to ensure comparability. Fluorescence signals were recorded in the DAPI channel (nuclei) and FITC channel (STAT-NF), and merged images were generated to visualize intracellular localization. Quantification of intracellular fluorescence intensity was performed using ImageJ, measuring mean fluorescence per cell across multiple fields and normalizing values to cell number.

2.10. Cellular uptake study and endocytosis inhibition of STAT and STAT-NF by confocal microscopy

Cellular uptake of fluorescent STAT and fluorescent STAT-NF was

qualitatively assessed by confocal laser scanning microscopy. For this purpose, MDA-MB-231 cells were seeded in 12-well culture plates at a density of $3x10^4$ cells/well and allowed to grow for 24 h. Subsequently, TNBC cells were treated for 1 and 2 h at 37 °C with STAT, conjugated with the fluorophore FAM (2.5 μM) and STAT-NF, conjugated with the fluorophore FAM (50 μM, *i.e.*, 2.5 μM of STAT), followed by appropriate washing and fixation steps [54]. For experiments on the inhibition of the endocytic pathway, MDA-MB-231 cells were pre-treated with 40 μM sodium azide for 30 minutes. After this, cells were then incubated for 1 and 2 hours with STAT (2.5 μM) and STAT-NF (50 μM, *i.e.*, 2.5 μM of STAT). In both experimental conditions, at the end of the treatments, samples were analysed by confocal microscope (Zeiss LSM 900 Airyscan 2) at 40× objective (oil immersion objective lens), to visualize nuclei (DAPI; 345/661 nm), STAT alone (AlexaFluor488; 493/519 nm) and STAT-NF (AlexaFluor488; 493/519 nm). All confocal images were examined and processed by ImageJ software. Intracellular fluorescence intensity was measured from Z-stack images, through a semi-quantitative image analysis approach and reported as the percentage of the fluorescence intensity of treated cells normalized to fluorescence intensity of non-treated cells.

2.11. Fluorescent detection of the apoptotic pathway

Detection of the programmed cell death apoptosis was evaluated by using a specific fluorescent apoptosis detection kit (Abcam, ab176749) [67]. Apoptotic cells were stained using Apopxin Green Indicator (Ex/Em = 490/525 nm), as a fluorescent sensor for phosphotidylserine (PS). For this purpose, MDA-MB-231 cells were grown in a black wall/clear bottom 96-well microplate (Corning Life Sciences, Bedford, U.S.A.) and treated or not with STAT (2.5 μM) and STAT-NF (50 μM, i.e., 2.5 μM of STAT) for 24 h. Doxorubicin (3 μM) was used as a positive drug for apoptosis induction. At the end of treatments, the cellular medium was replaced with a fresh one, to which appropriate quantities of reagent (PS sensor) were added, according to kit assay protocols. After 30 min of incubation (at RT, protected from light), cells were washed 2 times with assay buffer and then stained with DAPI (345/661 nm) as nuclear stain, and finally fixed with PFA (4%, 20 minutes). The fluorescence intensity was monitored at the indicated wavelengths by using a confocal microscope (Zeiss LSM 900 Airyscan 2) at 20× objective (oil immersion objective lens).

2.12. RT-qPCR analysis of STAT3 downstream genes

For gene expression analysis, MDA-MB-231 cells were seeded in 6-well plates and allowed to adhere for 24 h under standard culture conditions. Cells were then treated or not with STAT-NF (50 μM of STAT-NF, i.e. 2.5 μM of STAT) for 48 h. At the end of the incubation period, total RNA was extracted using an RNA extraction kit (Total RNA Purification Kit. NORGEN, Product # 17200) according to the manufacturer protocol.

Total cDNA was obtained using Applied Biosystems High-Capacity cDNA Reverse Transcription Kit (Cat. 4368814), and RT-qPCR was performed to evaluate the expression levels of c-MYC, Cyclin D1, and VEGFA, selected as representative genes involved in proliferation and angiogenesis. β-actin was used as the housekeeping gene for normalization. qPCR primers for human b-actin (Hs_ACTB_1_SG QuantiTect Primer Assay – GeneGlobe IdQT00095431), human cyclin D1 (rev: 5'-TCTGGCATTTTGGAGAGGAAGTG-3'; for: 5'-TCTACACCGACAACTCCATCCG-3'), human Bcl-2 (rev: 5'-CGGTTCAGGTACTCAGTCATTCC-3'; for:5'-GGTGGGGTCATGTGTGTGG-3') and human Bax (for: 5'-GTTTCATCCAGGATCGAGCAG-3', rev: 3'-CATCTTCTTCCAGATGGTGA-5'). Relative gene expression was calculated using the ΔΔCt method, and results were expressed as fold change compared with untreated controls.

2.13. Statistical data analysis

All experimental data were presented as mean values ± SEM. Statistical analysis was performed using one-way or two-way ANOVA followed by Dunnett's or Bonferroni's tests for multiple comparisons. GraphPad Prism 8.0 software was used for analysis. Differences between means were considered statistically significant when $p \leq 0.05$ was achieved.

3. Results and discussions

3.1. Multi-functionalization of the peptide-based nanofiber for STAT binding

3.1.1. Nanofiber design and functionalization

In our previous works, we designed two PAs (P1 and P2) endowed with intrinsic self-assembly capabilities, allowing them to arrange and form elongated nanostructures such as nanofibers [54–56]. To confer this self-assembling behavior, the PAs were equipped with a hydrophobic unit composed of a long lipid tail of nineteen carbon atoms (C19) and a sequence of six alanine (Ala_6), along with a charged domain including the anionic residue aspartic acid (in P1) and the cationic residues lysine and arginine (in P2) (Fig. 2). Upon co-assembly, these structural peptides, P1 and P2, generated a "naked" tubular structure characterized by a hydrophobic core and a large surface area, which can be readily functionalized according to the intended biological target.

In this work, the nanofiber surface was functionalized *ad hoc* for achieving a targeted and selective delivery of G4-aptamer STAT by integrating specific functional units, each contributing to a defined biological activity. For STAT binding on the nanofiber surface, we adopted a non-covalent conjugation strategy. Specifically, a six-arginine (R6) tail was attached to the N-terminus of the structural peptide P2, forming peptide P7, so that it would be exposed on the nanofiber surface and able to electrostatically interact with the negatively charged phosphate groups of STAT. [61]. In addition, to favor the intracellular internalization and promote STAT endosomal escape, we decorated the nanofiber with the cell-penetrating peptide gH625 (*sequence:* HGLASTLTRWAHYNALIRAF), able to cross the cell membrane mainly through a translocation mechanism that causes transient membrane destabilization without forming pores [58].

Instead, to confer cancer-cell selectivity, the peptide P22 (*sequence:* YHWYGYTPENVI) was employed to target and bind the EGFR receptor, commonly overexpressed in various tumor types [59]. To ensure that also gH625 and P22 were properly located on the exterior surface of the nanofiber, each of them was covalently conjugated to the structural peptide P2, yielding the peptides P3 and P6, respectively. This design enabled their stable incorporation into the nanofiber framework while orienting them outwardly, thereby preserving their biological functionality.

Moreover, all peptides were obtained using the Fmoc-based ultrasonic-assisted solid-phase peptide synthesis. Once the entire peptide sequence was achieved, lipidation was successfully performed by the conjugation of the C19 chain to the lysine side chain following mild acidic deprotection of the Mtt group. Then, all peptides were cleaved from the resin, purified, and recovered in their final form with good yields.

3.1.2. Nanofiber formulation and STAT complexation

The peptide self-assembly was assessed by fluorescence spectroscopy through the determination of the critical aggregation concentration (CAC) in water using the dye Nile Red, which migrates to hydrophobic environments created by the peptide amphiphiles when aggregated into nanofibers. For the construction of STAT-delivering nanofibers, a previously developed nanofiber composed of P1, P2, P3, and P6 at molar ratios of 50:42.5:5:2.5 was used as the starting platform [54]. The relative amounts of P3 (5%) and P6 (2.5%) were defined based on prior

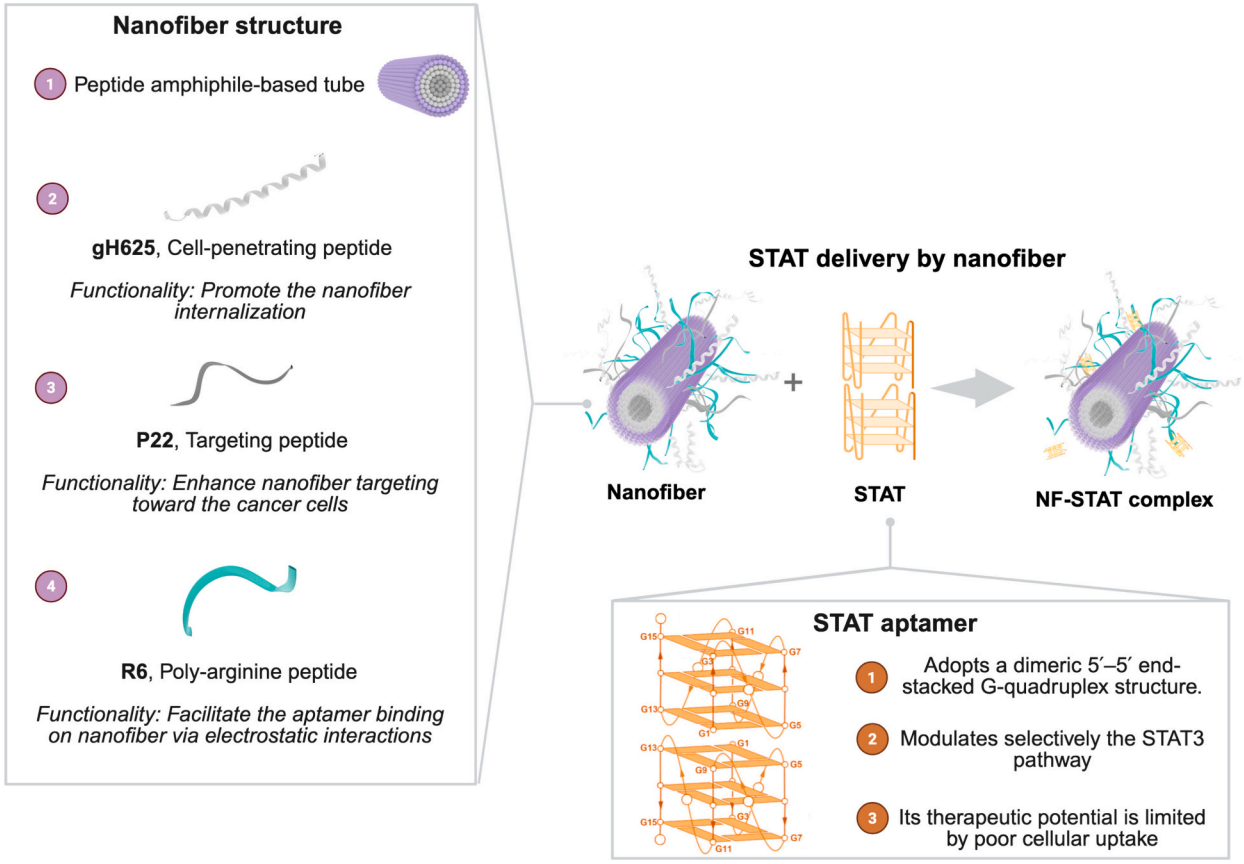

Fig. 1. Illustration of the nanofiber-aptamer complex. The nanofiber composition is illustrated, highlighting its constituent components on the surface, and the key structural features of the aptamer STAT are reported. The figure was created with BioRender.

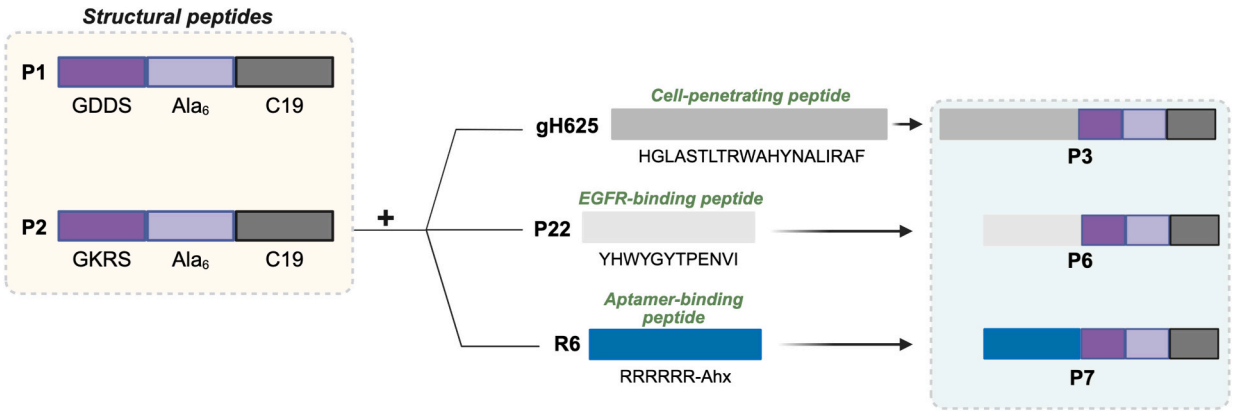

Fig. 2. Schematic illustration of the designed peptide sequences used for nanofiber construction.

biological evaluations, accounting for their penetration and targeting functionalities, respectively. The assembly of the peptides P1, P2, P3, and P6 at these molar ratios resulted in a CAC value of 17.3±0.2 μM, and nanofiber formation with an average length of 230±50 nm and a diameter of approximately 10 nm was confirmed by transmission electron microscopy [54].

For STAT binding, the peptide amphiphile P7, bearing a hexa-arginine tail, was selected to enable electrostatic interactions with the negatively charged phosphate backbone of the 16-mer STAT aptamer. Two nanofiber preparations containing two different percentages of P7 10% and 20% were prepared for evaluating STAT complexation. Firstly, CAC values of both nanoformulations were determined (Table 2). Nile Red fluorescence assays revealed that incorporation of the hydrophilic R6 tail markedly enhanced the aggregation propensity, promoting nanofiber formation at lower concentrations. Accordingly, CAC values of 11.6 ± 0.2 μM and 6.1 ± 0.1 μM were calculated for NF-P7 (10%) and NF-P7 (20%), respectively. Additionally, dynamic light scattering (DLS)

Table 2
Summary of biophysical data of nanofiber formulations

Formulation	Peptide ratio	CAC (μM)	Zeta potential (mV)
NF (10% P7)	P1:P2:P3:P6:P7 (50:32.5:5:2.5:10)	11.6 ± 0.2	+ 9.1±0.5
NF (20% P7)	P1:P2:P3:P6:P7 (50:22.5:5:2.5:20)	6.1 ± 0.1	+14.2±2.4

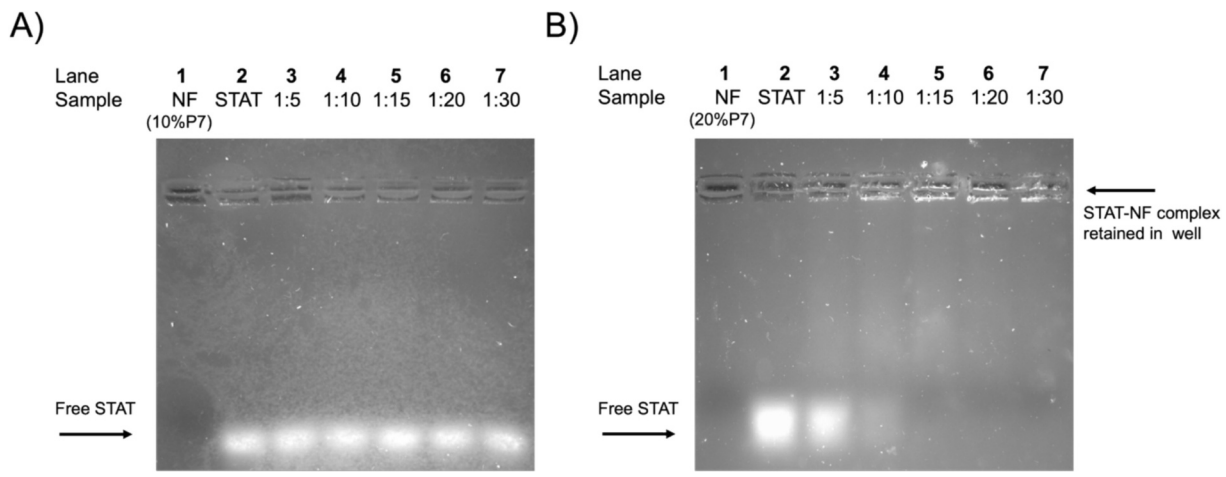

Fig. 3. Electrophoresis performed for nanofibers decorated with 10 % (panel A) and 20 % (panel B) P7 and STAT in various STAT:NF ratios. Samples containing 1 μM STAT per lane and nanofibers applied in the corresponding concentrations were prepared in water in the presence of GelRed stain. Gels were visualized upon transillumination at 525 nm. Lane 1: STAT alone (control); Lane 2: nanofiber alone; Lanes 3-7: STAT incubated with increasing NF concentrations (indicated as STAT: NF ratios of 1:5, 1:10, 1:15, 1:20, 1:30).

analysis confirmed that both nanoformulations exhibited a positively charged surface necessary for the STAT binding. Specifically, we measured a zeta potential of +9.1±0.5 and +14.2±2.4 mV for the NF (P7 10%) and NF (P7 20%), respectively. This difference in zeta potential can be attributed to the different concentrations of the positively charged peptide P7.

At this stage, the optimal P7 amount for STAT binding to the nanofiber was determined by agarose gel electrophoresis. To validate the complexation, the aptamer was incubated with NF (P7 10%) and NF (P7 20%) at the STAT:NF molar ratios of 1:5, 1:10, 1:20, and 1:30 for 30 min. The resulting complexes were then analyzed by gel electrophoresis, alongside control samples consisting of STAT alone and nanofiber alone (Fig. 3).

As shown in Fig. 3A, no appreciable binding between STAT and NF-P7 (10%) was observed across the tested molar ratio range, likely due to an insufficient P7 content to effectively bind the negative charges of the aptamer.

In contrast, the NF decorated with 20% P7 was able to bind STAT with aptamer complexation progressively increasing as the STAT:NF ratio increased (Fig. 3B). Specifically, the complex started forming at the ratio 1:10 (STAT:NF) and the fluorescence band disappeared at a molar ratio of 1:20. Based on these findings, the nanofiber formulation containing 20% P7 (referred to as NF from now) was selected as the most effective formulation for STAT binding and delivery, and the STAT:NF molar ratio of 1:20 was chosen for subsequent biological evaluations.

3.1.3. Physicochemical characterization of the nanofiber

The NF decorated with 20% P7 was characterized in terms of size, morphology, and structural stability. The size and morphology of NF were investigated by scanning electron microscopy (SEM) analysis, revealing the formation of a nanofiber network with an average length of fibers of 100±30 nm and a diameter of 25±5nm (Fig. 4A).

Moreover, to investigate the secondary structure of NFs, we employed circular dichroism (CD) spectroscopy. As observed in Fig. 4B, NFs adopt a β-sheet conformation with a minimum at approximately 215 nm. Notably, this secondary structure was preserved under dilution (50, 40, 30, and 10 μM; Fig. 4B), increasing ionic strength in the presence of sodium chloride (NaCl, up to 10 mM, Fig. 4C), and in acidic conditions (pH 5; Fig. 4D).

3.2. Biophysical characterization of STAT-NF complex

The binding between STAT and the polyarginine-peptide sequence R6 exposed on NF's surface has been further characterized with DLS, fluorescence and CD spectroscopies.

First, the changes in the surface charge of STAT upon complexation with NFs at different molar ratios were evaluated by DLS through zeta potential measurements. STAT alone exhibited a negative zeta potential (−26.2 mV) in buffer, which progressively increased upon rising NF amount (Fig. 5A). The zeta potential remained negative at low STAT:NF ratios (1:5 and 1:10), whereas a positive surface charge was observed at higher ratios (1:20 and 1:30). Notably, the most marked increase in zeta potential occurred at a STAT:NF ratio of 1:30 (+10 mV), thus indicating complete neutralization of the negatively charged phosphate groups of STAT by the nanofiber.

Moreover, the interaction between STAT and NF was also studied by fluorescence spectroscopy by exciting STAT at 260 nm and recording the emission spectrum in the 350-500 nm range. Upon addition of NF, a pronounced blue shift accompanied by a significant increase in fluorescence quantum yield was observed, particularly at STAT:NF molar ratios of 1:20 and 1:30 (Fig. 5B). These spectral changes suggest a modification of the local microenvironment of STAT due to the presence of NF.

We also investigated the structural stability of the aptamer STAT upon the NF complexation by CD analysis. STAT adopts a G4 structure characterized by a minor band at 242 nm and a major positive band at 263 nm [11]. Upon the nanofiber complexation at the different STAT:NF ratios, these bands were preserved. Although a decrease in ellipticity intensity was observed, no shifts in peak positions occurred, indicating that STAT preserves its G4 conformation upon binding to the nanofiber (Fig. 5C). The presence of the G4-conformation was further detected using the Thioflavin T (ThT) probe. Upon binding to G4-structures, ThT exhibits a marked enhancement of fluorescence emission at approximately 490 nm, whereas significantly lower fluorescence is observed in the presence of single- or double-stranded oligonucleotides [68]. As shown in Fig. 5D, incubation of ThT with STAT resulted in a pronounced increase in fluorescence intensity at ~490 nm compared to ThT alone. Notably, the addition of ThT to the STAT:NF (1:20) complex did not lead to a significant reduction in fluorescence intensity; instead, the emission

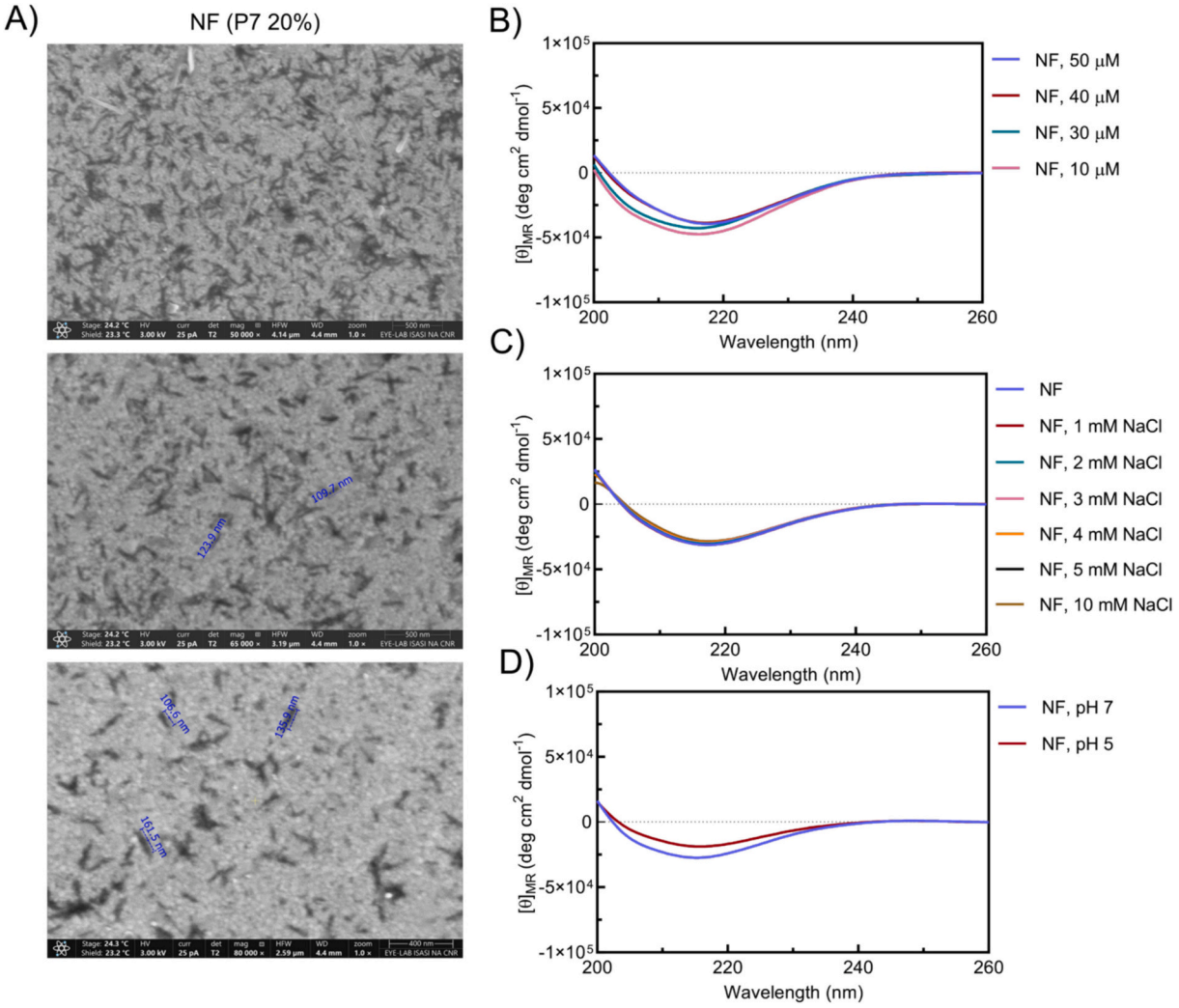

Fig. 4. Panel A: SEM images of NF (P7 20%). Panels B, C and D: Structural stability of NF under dilution effect (B), ionic strength (C) and pH environments (D), respectively.

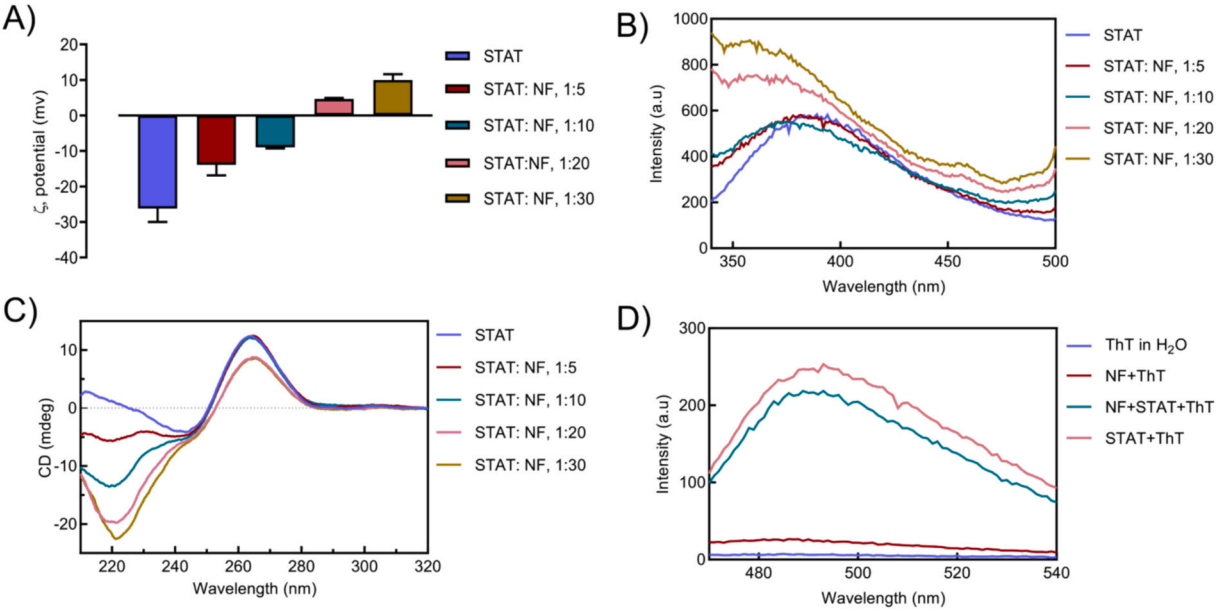

Fig. 5. Panel A: Zeta potential values at the various ratios STAT:NF. Panel B: STAT fluorescence spectra before and after the complexation with NF at different ratios. Panels C: CD spectra of STAT alone and after the complexation with NF at different ratios. Panels D: ThT fluorescence spectra before and after the complexation between NF and STAT.

profile closely resembled that observed for STAT alone. These results indicate that the G4-conformation of STAT is preserved upon binding to the nanofiber.

3.3. Stability of the STAT-NF complex

The stability of the STAT-NF complex was assessed by CD measurements under different conditions, including time, temperature, and ionic strength. The STAT:NF complex was prepared at a 1:20 molar ratio, and its stability was monitored over time at room temperature by circular dichroism spectroscopy. As shown in Fig. 6A, no appreciable changes in the CD signal were observed at the different time points examined, indicating that at 25 °C the complex remains structurally stable for at least 24 h. In addition to its stability at room temperature, the STAT-NF complex kept its structural integrity as STAT alone at physiological temperature (37 °C) as well as under elevated thermal conditions (45 °C and 60 °C) (Fig. 6B–6C). No significant alterations in the CD signal of the STAT-NF complex were detected at these temperatures (Fig. 6B), indicating that the STAT-NF interaction is thermally robust.

However, since ionic strength and salts can influence the stability of noncovalent interactions, we explored the effect of different concentrations of sodium chloride on STAT-NF complex.

Sodium chloride was added to STAT-NF complex, prepared at a 1:20 molar ratio, at concentrations ranging from 1 to 10 mM, and the resulting structural stability was evaluated by CD. As shown in Fig. 6D-6E, no significant alterations in the CD spectra were observed across this range of ionic strengths as well as STAT alone, indicating that STAT-NF complex remains structurally stable under these conditions.

3.4. Antiproliferative activity on breast cancer cells

The antiproliferative activity of STAT alone and EGFR-targeted STAT-NF, *ad hoc* delivered by the nanofiber, was evaluated on a limited panel of specific phenotypes of human breast cancers, appropriately selected since they overexpress epidermal growth factor (EGF) receptors (EGFRs). Among the BC preclinical models tested, TN MDA-MB-231 cells were the most sensitive to STAT-NF exposure. In fact, cellular responses by the analysis of "cell survival index" (Fig. 7), showed significant cytotoxic effects in MDA-MB-231, at the highest tested concentration (2.5 μM) after 48 h and at all the tested concentrations after 72 h of incubation.

Conversely, under the same experimental conditions, STAT alone did not induce any significant biological effects, even at the longest exposure times and highest concentrations tested.

On a different note, a mild but significant effect on cellular viability was also observed in T47D cells after 72 h of incubation with STAT-NF, whereas STAT alone was bioactive only at the highest concentration tested.

Additionally, under the same experimental conditions, no significant cellular responses were observed in healthy fibroblast control cells (HDFa line) at all tested concentrations after 48 and 72 h of incubation. Furthermore, no significant cytotoxicity was observed in all cellular

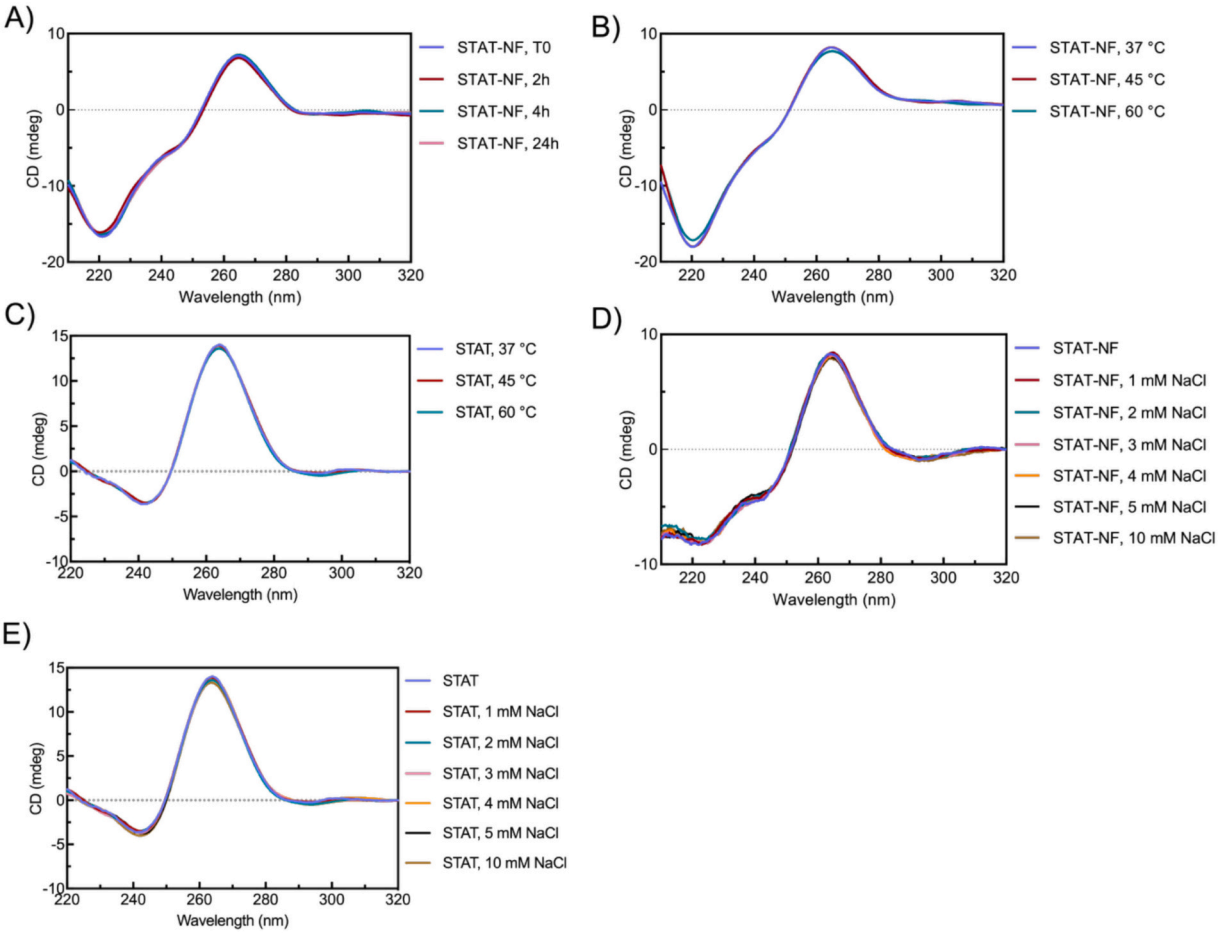

Fig. 6. Panel A: The stability of the STAT-NF complex (at the ratio 1:20) over time at 25 °C. Panels B–E: The stability of STAT-NF and STAT alone at different temperatures (B, C) and varying ionic strength (D, E).

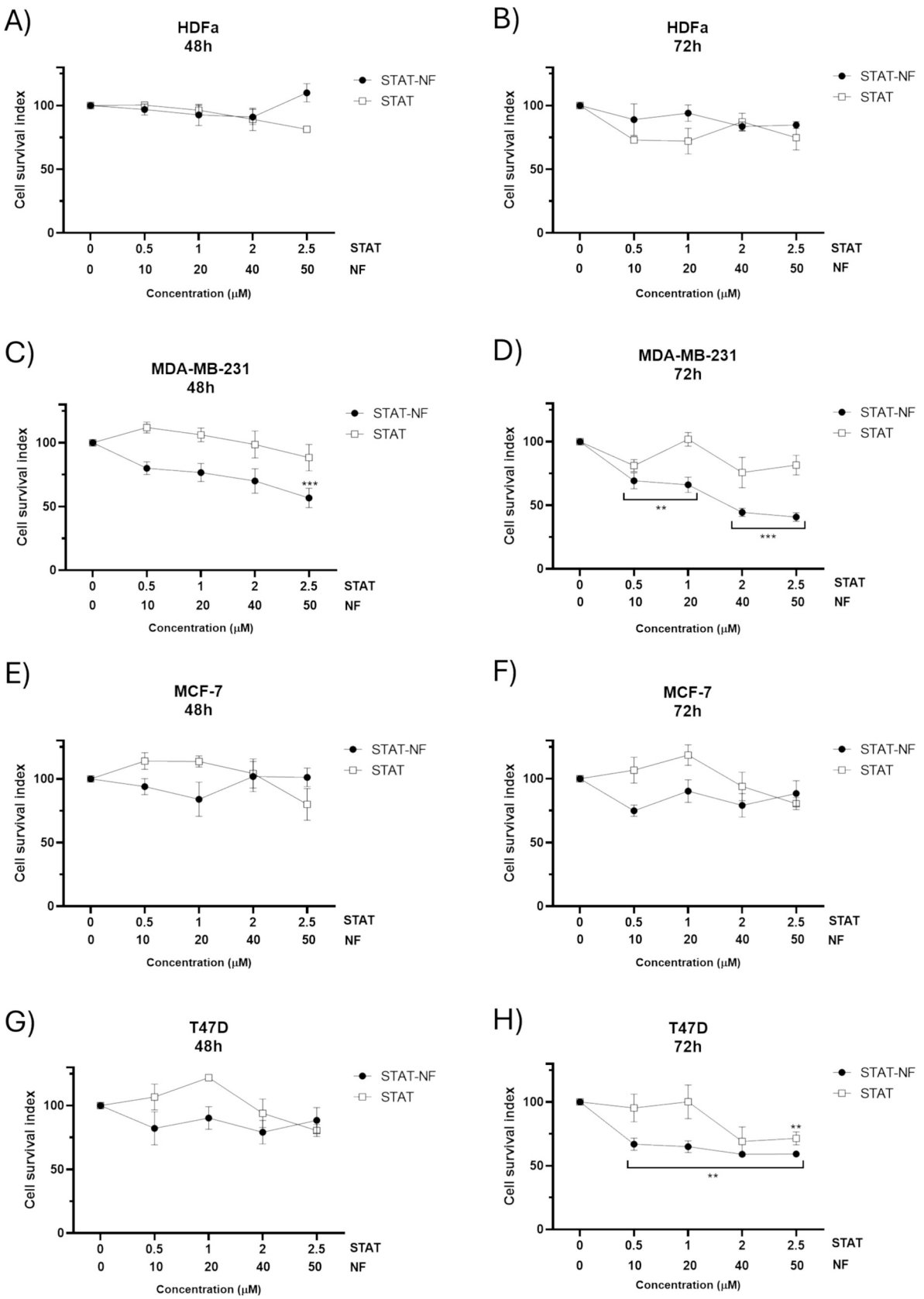

Fig. 7. Cell survival index, evaluated by the MTT assay and live/dead cell ratio analysis, for human triple negative breast cancer cells MDA-MB-231 (C and D), human epithelial like breast cancer cells MCF-7 (E and F), human epithelial like breast cancer cells T47D (G and H) and human dermal fibroblast HDFa (A and B) following 48 and 72 h of incubation with STAT-NF (concentration range 10 → 50 μM of NF; *i.e.* concentration range 0.5 → 2.5 μM of STAT) and STAT (concentration range 0.5 → 2.5 μM), as indicated in the legend. Data in line graphs are expressed as percentages of untreated control cells and are reported as mean of 3 independent experiments ± SEM (n = 12). ** $p < 0.01$ vs. control cells; *** $p < 0.001$ vs. control cells.

lines used, even at the highest tested concentration (50 μM) after 72 h of incubation of the unloaded NF (Fig. S13).

The most significant cytotoxic effect associated with STAT, cropped up from this analysis, marked only when this aptamer was *ad hoc* administered *via* NF, suggesting a limited cellular uptake of STAT alone. Moreover, the stronger response detected in MDA-MB-231 cells compared with EGFR-low model, such as MCF-7 cell line, suggests a preferential activity toward EGFR-overexpressing phenotypes, consistent with their higher ability to internalize the NF-delivered aptamer.

3.5. Selective uptake in EGFR-High and EGFR-low breast cancer cells

To assess the EGFR-dependent selectivity of the NF-mediated delivery system, we performed a fluorescence-based uptake analysis using FITC-labeled STAT-NF in EGFR-high and EGFR-low breast cancer cells. Fluorescence microscopy revealed a marked difference in the internalization of STAT-NF between the two breast cancer models. In MDA-MB-231 cells, characterized by high EGFR expression, incubation with STAT-NF (FITC-labeled) for 2 h resulted in a strong intracellular green fluorescence signal, clearly detectable in Fig. 8A. In contrast, MCF-7 cells displayed a minimal internalization of STAT-NF, under the same experimental conditions, consistent with their low EGFR expression (Fig. 8B). Quantification of intracellular fluorescence intensity, shown in Fig. 8C, confirmed these observations, showing a significantly higher uptake in MDA-MB-231 cells compared with MCF-7 cells. These data support a receptor-dependent internalization mechanism and are consistent with the preferential biological activity observed in EGFR-overexpressing phenotypes.

3.6. Study of the mechanism of nanofibers internalization

To elucidate the cellular internalization mechanisms of STAT, uptake investigations were performed in TNBC for both the aptamer alone and its nanofiber-associated formulation (STAT-NF). To discriminate between passive or non-endocytic internalization and active endocytosis-dependent mechanisms, *in vitro* uptake experiments were conducted under standard conditions as well as in the presence of endocytosis inhibition.

Confocal time-course microscopy experiments at 1 and 2 hours showed marked cellular uptake of STAT-NF (green fluorescence) already at 1 hour of incubation (as shown in supplementary in Fig. S14), which became significant after 2 hours (Fig. 9), under endocytic standard conditions. In this context, analysis of three representative Z-stack sections, reported in supplementary (Fig. S15), revealed a significant intracellular localization of STAT, characterized by an intense and broadly cytoplasmic fluorescence signal. In contrast, fluorescence intensity was barely detectable after 2 hours of treatment with STAT alone, indicating poor cellular uptake of the aptamer when not properly delivered (Fig. 9). This finding is consistent with the *in vitro* cytotoxicity outcome.

In parallel, Fig. 10 reveals that, under endocytosis inhibition using sodium azide, the internalization of STAT *via* NF was not significantly altered compared to STAT alone, which showed a markedly decreased fluorescence intensity signal (Fig. 10B). These results confirm our previous data, indicating that gH625 promotes a translocation across the membrane which only partially involves endocytic mechanisms [54,58]. In contrast to most conventional nanosystems that are primarily internalized through endocytosis and often remain entrapped within endosomal vesicles, the presence of gH625 helps to overcome the endosomal entrapment limitation, as cellular internalization occurs predominantly via a translocation mechanism.

Moreover, alterations in uptake trafficking pathways have been implicated in chemoresistance mechanisms in cancer cells, potentially affecting drug uptake and then its therapeutic efficacy [69]. In this context, the evidence that STAT-NF cellular uptake was effective even under conditions of endocytosis inhibition suggests that the nanofiber-mediated delivery can bypass classical endocytosis-dependent limitations, potentially contributing to reduced therapeutic efficacy in resistant cancer cells.

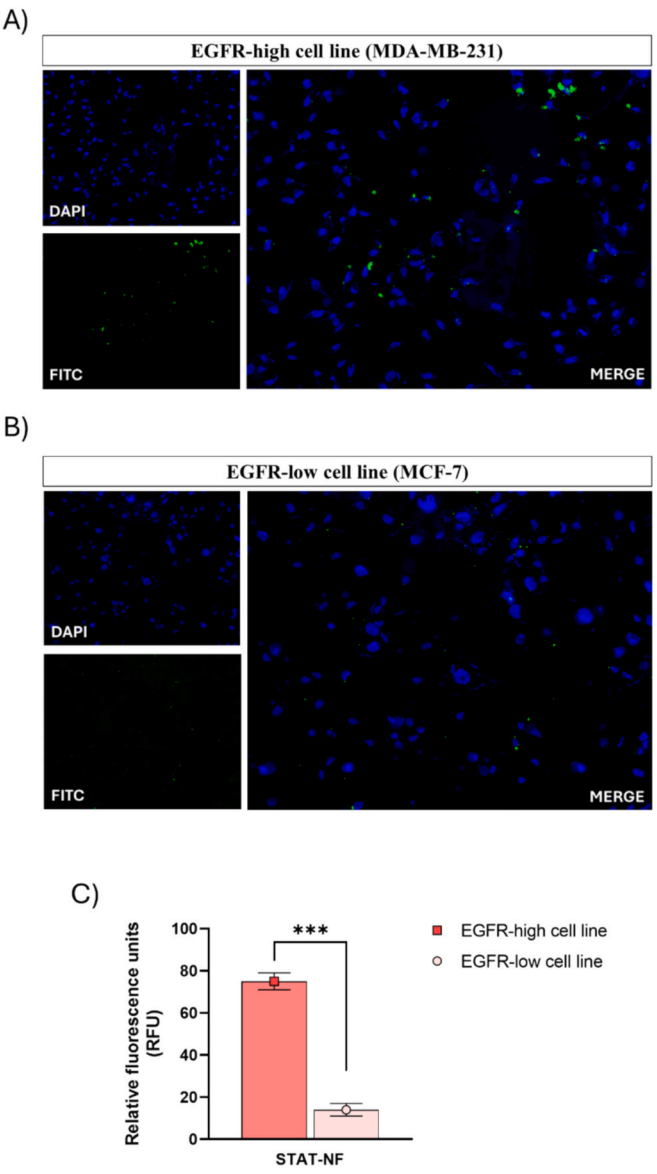

Fig. 8. Cellular uptake of STAT-NF in (A) EGFR-high cell line MDA-MB-231 and (B) EGFR-low cell line MCF-7, assessed after 2 h of incubation with 50 μM of STAT-NF (i.e. 2.5 μM of STAT). Cellular nuclei are stained blue (DAPI filter, Ex/Em = 350/470 nm), and fluorescent STAT was detected by green fluorescence (FITC, Ex/Em = 488/530 nm). Images were acquired by fluorescent microscopy at 10× magnification. (C) Fluorescence intensity values were normalized to control cells and expressed as relative units (RFU). Data are shown as mean ± SEM. ***$p<0.001$ vs. control cells.

3.7. Apoptosis activation

Since apoptosis represents one of the principal regulated cell death (RCD) pathways induced by canonic chemotherapeutic or cytotoxic agents, targeted experiments were carried out to study the activation of

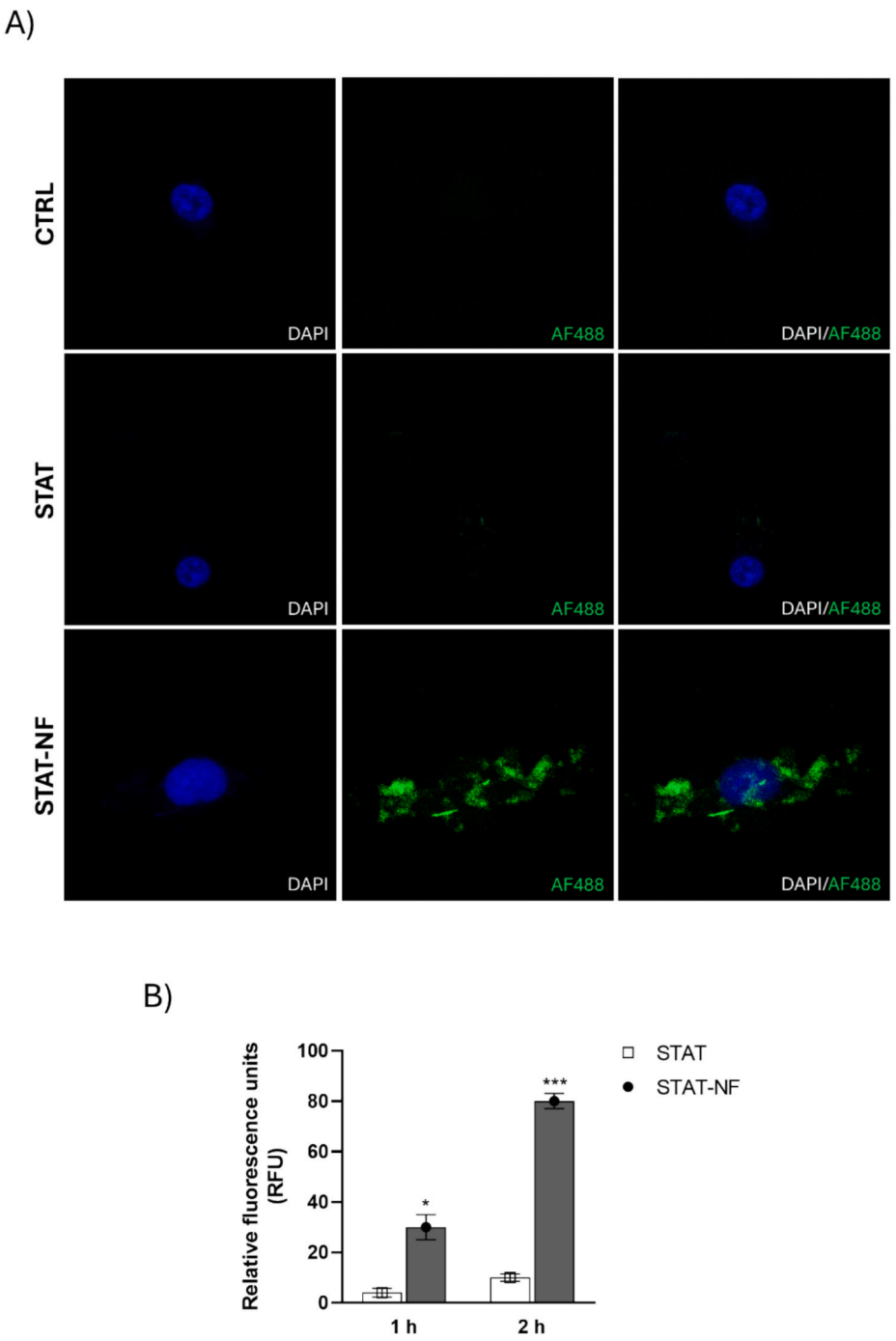

Fig. 9. (A) Cellular uptake of STAT and STAT-NF aptamers in MDA-MB-231 TNBC cells assessed after 2 h of incubation with 2.5 μM of STAT and 50 μM of STAT-NF (*i.e.*, 2.5 μM of STAT), under endocytic standard conditions. Cellular nuclei are stained blue (DAPI filter, Ex/Em = 350/470 nm), and fluorescent STAT was detected by green fluorescence (AF488, Ex/Em = 493/519 nm). Images were acquired by confocal microscopy at 40× magnification (oil immersion lens). (B) Fluorescence intensity values after 1 and 2h of STAT and STAT-NF cellular incubation were normalized to control cells and expressed as relative units (RFU). Data are shown as mean ± SEM. *$p<0.05$; ***$p<0.001$ vs. control cells.

the apoptotic pathway in the MDA-MB-231 cell line following exposure to STAT *via* NF (STAT-NF) or not (STAT alone).

Confocal microscopy photographs, depicted in Fig. 11, revealed the activation of the early apoptosis pathway (marked in fluorescent green) after 24 h of STAT-NF incubation. The observed effect was significant and comparable to that of doxorubicin (Dox), used as a positive control for apoptosis induction. As expected, due to a limited cellular uptake, STAT alone-treated cells did not show significant signs of activation of this cell death pathway.

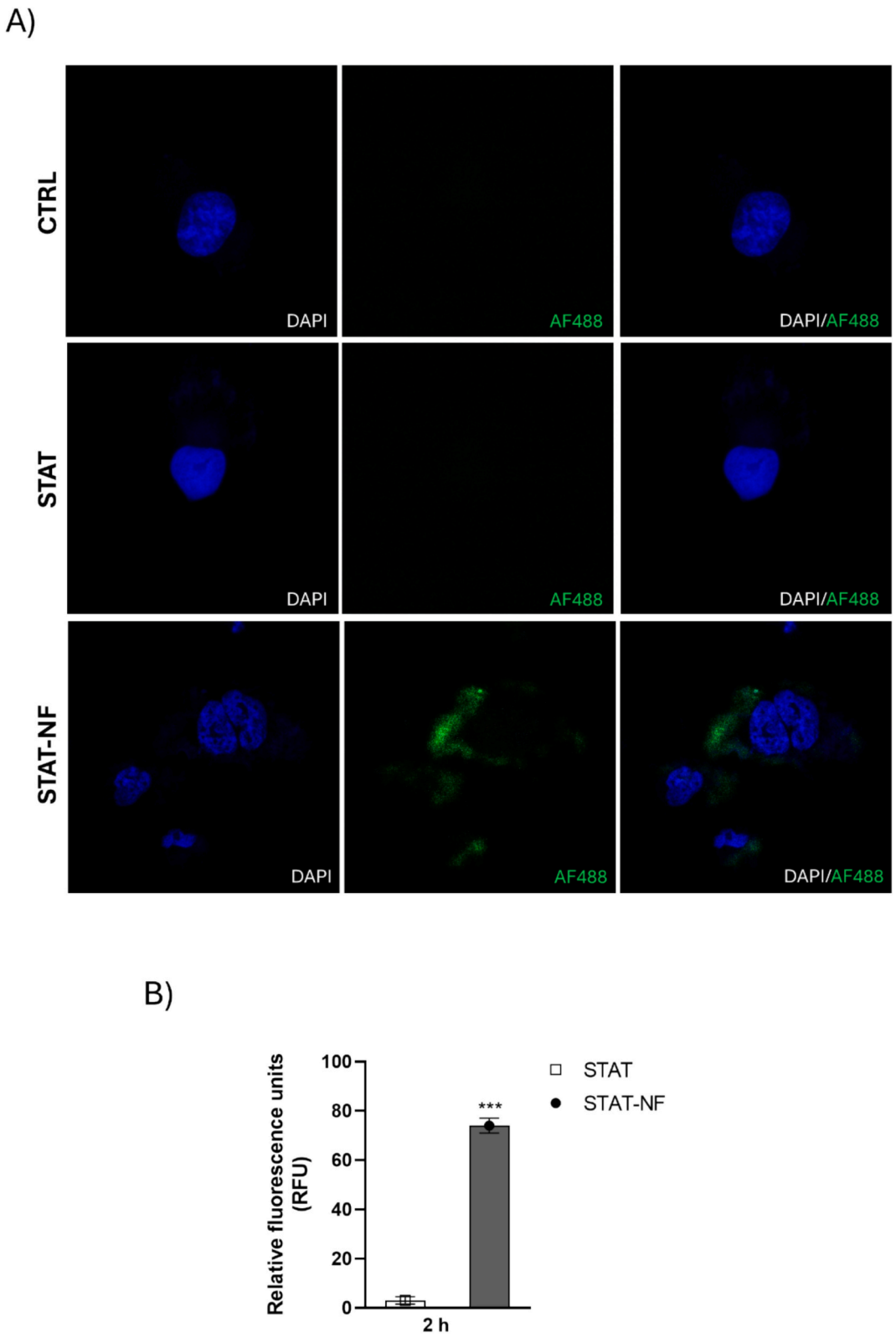

Fig. 10. (A) Cellular uptake of STAT and STAT-NF aptamers in MDA-MB-231 TNBC assessed after 2 h of incubation with 2.5 μM of STAT and 50 μM of STAT-NF (i.e., 2.5 μM of STAT), under endocytic inhibition conditions. Cellular nuclei are stained blue (DAPI filter, Ex/Em = 350/470 nm), and fluorescent STAT was detected by green fluorescence (AF488, Ex/Em = 493/519 nm). Images were acquired by confocal microscopy at 40× magnification (oil immersion lens). (B) Fluorescence intensity values after 2h of STAT and STAT-NF cellular incubation were normalized to control cells and expressed as relative units (RFU). Data are shown as mean ± SEM.***$p<0.001$ vs. control cells.

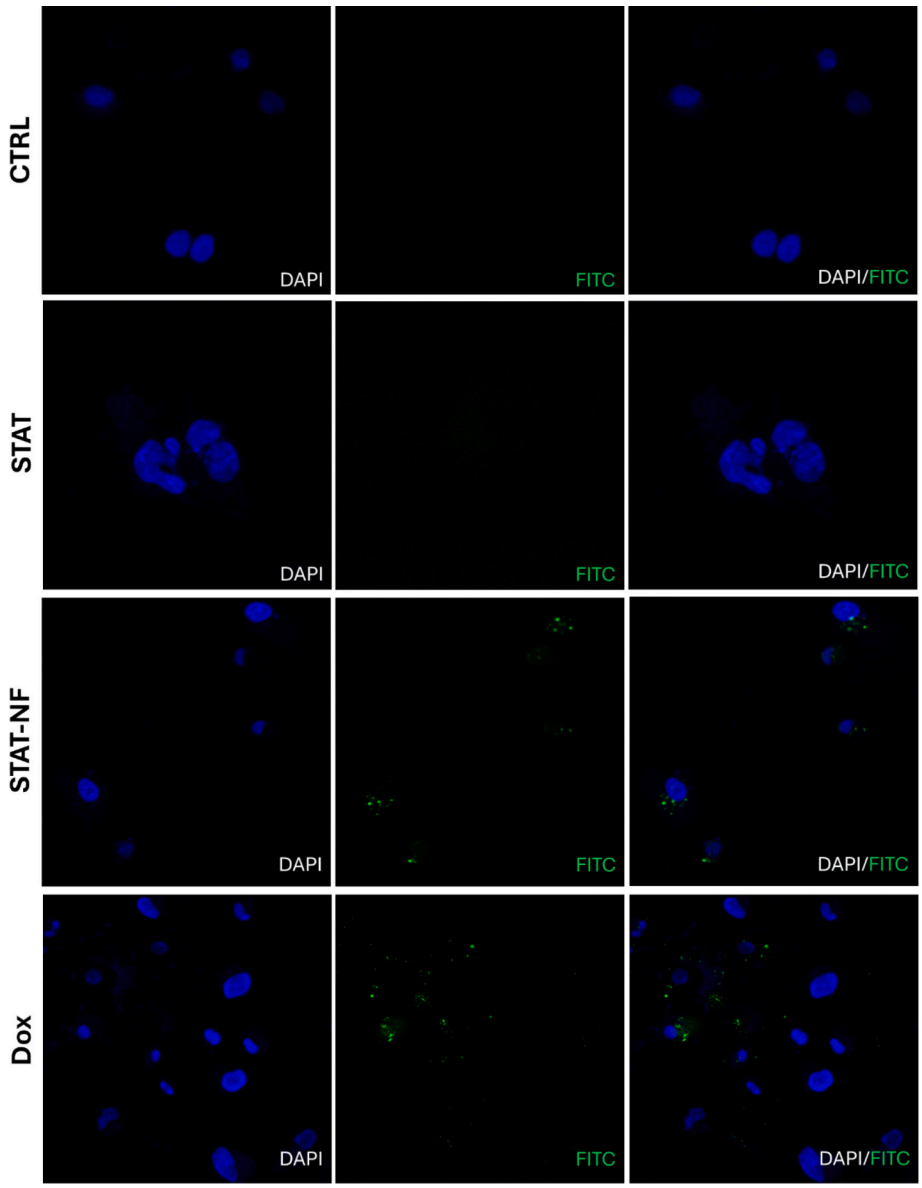

Fig. 11. Apoptosis induction in MDA-MB-231 cells was assessed after 24 h incubation with STAT (2.5 μM), STAT-NF (50 μM; *i.e.*, 2.5 μM of STAT) and Doxorubicin (Dox, 3 μM). Cell nuclei are stained blue (DAPI filter, Ex/Em = 350/470 nm), and apoptotic cells are identified by green fluorescence due to phosphatidylserine (PS) binding (FITC, Ex/Em = 490/525 nm). Images were acquired at 20× magnification.

3.8. Modulation of STAT3-regulated genes in MDA-MB-231 cells

To determine whether STAT-NF treatment impacted the transcriptional program downstream of STAT3, the expression of key STAT3-regulated genes was evaluated in MDA-MB-231 cells after 48 h of exposure. RT-qPCR analysis revealed a significant reduction in Cyclin D1 and Bcl-2 mRNA levels in STAT-NF–treated cells compared to untreated controls (Fig. 12). The decrease in these transcripts, normalized to β-actin, indicates an effective suppression of STAT3-dependent proliferative pathways. Conversely, the regulation of Bax transcription shows a significant increase in mRNA levels. These findings are consistent with the antiproliferative and pro-apoptotic effects observed in MDA-MB-231 cells and support the functional impact of nanofiber-mediated STAT delivery on STAT3 signaling.

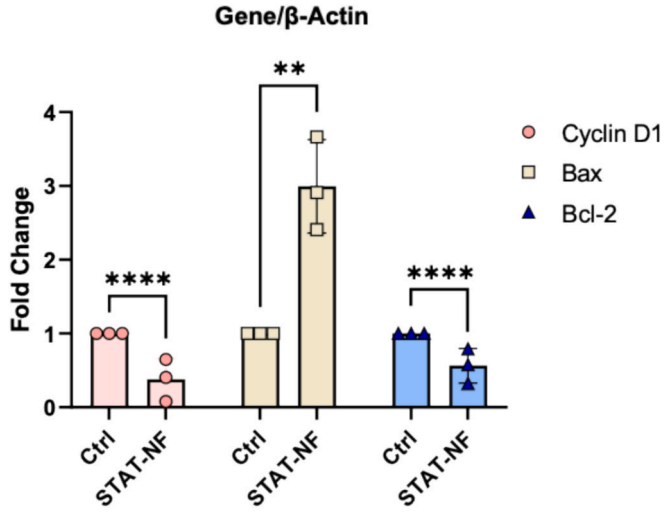

Fig. 12. Relative mRNA expression levels of STAT3 downstream genes (Cyclin D1, Bax and Bcl-2) in MDA-MB-231 cells after 48 h of STAT-NF treatment (50 μM of STAT-NF, *i.e.* 2.5 μM of STAT). Genes expression was quantified by RT-qPCR and normalized to β-actin. Fold change values were calculated using the ΔΔCt method and expressed relative to untreated controls (set to 1). Data are presented as mean ± SEM.****p<0.0001 vs control cells; ** p < 0.01 vs. control cells.

4. Conclusions

In this study, we developed a multifunctional peptide-based nanofiber platform specifically engineered for the efficient delivery of the G4-aptamer STAT in breast cancer cells. G4 structures are highly charged and conformationally rigid nucleic acids that, because of their physicochemical properties, exhibit poor membrane permeability and are therefore inefficiently internalized when administered alone. As a result, the delivery of G4-aptamers remains a major challenge. Moreover, following cellular uptake, G4s are frequently sequestered within endosomal compartments, limiting access to their intracellular targets. Preservation of the native G4 conformation during delivery is also essential for biological activity, as structural destabilization can impair target recognition and therapeutic efficacy. Collectively, these problems underscore the need for advanced delivery systems capable of protecting G4-structures, promoting cellular uptake, enabling cytosolic release, and maintaining functional folding. To address these limitations, we designed peptide nanofibers that safely, efficiently, and selectively deliver G4-aptamers to target cancer cells. This platform is biocompatible, modular, and readily scalable, and its rational surface functionalization enables stable STAT complexation, enhanced cellular internalization, and tumor selectivity, thereby unlocking the therapeutic potential of G4-based nucleic acid therapeutics.

The incorporation of a surface-exposed polyarginine (R6) motif proved essential for effective electrostatic binding of STAT while preserving its G4-conformation and ensuring complex stability under physiologically relevant conditions. In particular, we demonstrated that the inclusion of 20% R6-containing peptide (P7) conferred a positive zeta potential to the nanofibers and enabled efficient STAT binding, with aptamer complexation progressively increasing as the STAT:NF molar ratio increased, and reaching complete binding at a 1:20 ratio. Morphological characterization revealed the formation of a well-defined nanofiber network with an average fiber length of 100 ± 30 nm and a diameter of 25 ± 5 nm, consistent with a stable supramolecular architecture. Circular dichroism analyses demonstrated that the nanofiber secondary structure was preserved under dilution, increased ionic strength, and acidic conditions, confirming the structural robustness of the system and its suitability for biological environments.

The stability of the STAT-NF complex was further evaluated under varying conditions of time, temperature, and ionic strength, demonstrating that the complex remains intact prior to reaching the cellular target.

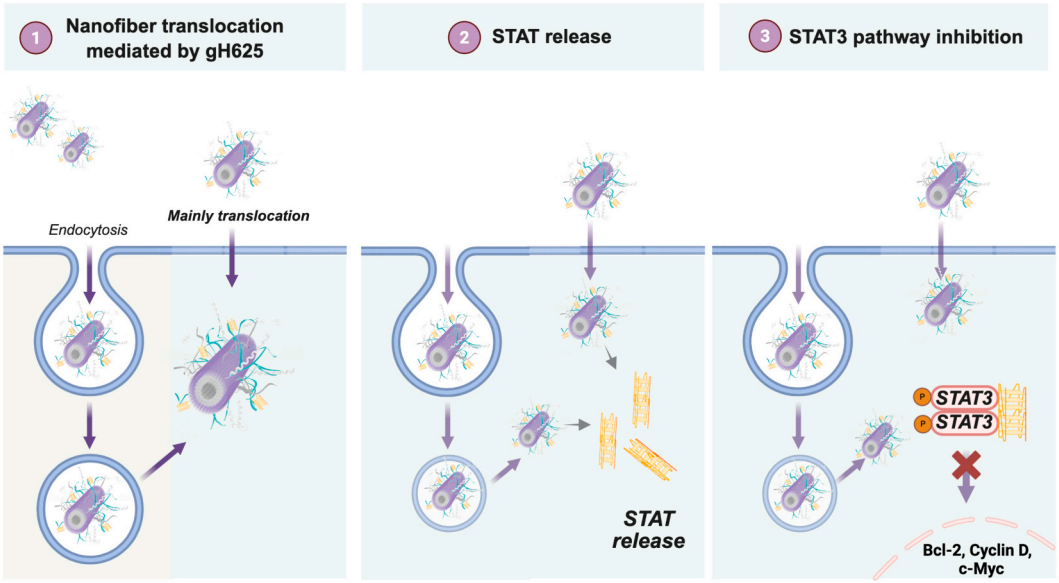

Fig. 13. Schematic representation of the proposed mechanism of action of the STAT-NF complex.

Mechanistic studies further revealed that STAT-NF internalization occurs predominantly through an endocytosis-independent translocation mechanism, thereby overcoming classical uptake limitations and enabling efficient intracellular delivery (Fig. 13). This behavior is granted by the presence of gH625, a cell-penetrating peptide developed in our laboratory, which facilitates translocation across cellular membranes while only partially engaging endocytic pathways. Importantly, modulation of the uptake mechanism may represent an effective strategy to circumvent resistance mechanisms and enhance therapeutic efficacy.

Consistent with these findings, nanofiber-mediated delivery markedly enhanced STAT cellular uptake compared with the free aptamer, even under conditions of endocytosis inhibition. This improved internalization translated into a significant and selective antiproliferative effect in triple-negative breast cancer cells, with negligible toxicity toward healthy cells. Ultimately, NF-mediated STAT delivery induced apoptosis activation, underscoring the therapeutic relevance of this approach. Moving in this direction, the analysis of STAT3 downstream genes involved in the regulation of dynamic cellular processes, such as proliferation and activation of RCDs pathways highlights promising clinical potential. In this context, the Bax/Bcl-2 ratio predisposing cells toward the activation of apoptosis, is very interesting.

Overall, this work advances our understanding of peptide-based nanofibers as a modular, versatile and effective platform for aptamer delivery. These results together with future *in vivo* studies may provide new strategies to enhance the intracellular bioavailability and anticancer efficacy of nucleic acid therapeutics.

CRediT authorship contribution statement

Rosa Bellavita: Writing – original draft, Methodology, Investigation, Conceptualization. **Daniela Benigno:** Writing – original draft, Methodology, Data curation. **Marialuisa Piccolo:** Writing – original draft, Visualization, Data curation. **Simone Braccia:** Methodology, Data curation. **Carla Aliberti:** Methodology, Data curation. **Federica Iazzetti:** Methodology, Data curation. **Antonella Virgilio:** Investigation, Conceptualization. **Veronica Esposito:** Investigation, Conceptualization. **Federica Donadio:** Methodology, Data curation. **Emanuela Esposito:** Visualization, Data curation. **Antonio Giordano:** Writing – original draft, Supervision. **Annarita Falanga:** Methodology, Investigation, Conceptualization. **Carlo Irace:** Writing – original draft, Supervision. **Aldo Galeone:** Investigation, Funding acquisition, Conceptualization. **Stefania Galdiero:** Writing – original draft, Visualization, Methodology, Investigation, Funding acquisition, Conceptualization.

Declaration of competing interest

All authors state that there are no competing interest to declare.

Acknowledgements

This work was financially supported by “CN00000041 “National Center for Gene Therapy and Drugs based on RNA Technology” (concession number 1035 of 17June 2022-PNRR MUR- M4C2-Investment1.4 Call “NationalCenters”, financed by the EU- NextGenerationEU), code project MUR: CN00000041-CUP UNINA: E63C22000940007, and the European Union-NextGenerationEU-PNRR MUR-PRIN 2022-[CUP UNINA: E53D23009940006]. R.B. and S.G. are grateful to CN00000041 “National Center for GeneTherapy and Drugs Based on RNA Technology”. D.B. holds a research contract (art. 22 L. 240/2010 CUP: E63C25000640004) under the framework of the Piano Nazionale di Ripresa e Resilienza (PNRR)- Avviso MUR D.D. n. 47 del 20/02/2025 - Missione 4-Componente 2-Investimento 1.2 “Finanziamento di progetti presentati da giovani ricercatori”. S.B. acknowledges support from a fellowship within the framework of the Department of Excellence program at the Department of Pharmacy. We gratefully acknowledge Prof. Carla Langella and Dr. Giovanna Nichilò for their contribution to the creation of Fig. 1.

Appendix A. Supplementary data

Supplementary data to this article can be found online at https://doi.org/10.1016/j.ijbiomac.2026.152317.

Data availability

Data will be made available on request.

References

[1] C. Roxo, W. Kotkowiak, A. Pasternak, G-Quadruplex-Forming Aptamers-Characteristics, Applications, and Perspectives, Molecules 24 (2019) 3781.
[2] H. Sun, X. Zhu, P.Y. Lu, R.R. Rosato, W. Tan, Y. Zu, Oligonucleotide aptamers: new tools for targeted cancer therapy, Mol. Ther. Nucleic. Acids. 3 (2014) e182.
[3] A. Cucchiarini, M. Dobrovolna, V. Brazda, J.L. Mergny, Analysis of quadruplex propensity of aptamer sequences, Nucleic, Acids. Res. 53 (2025) gkaf424.
[4] D. Song, J. Luo, X. Duan, F. Jin, Y.J. Lu, Identification of G-quadruplex nucleic acid structures by high-throughput sequencing: A review, Int. J. Biol. Macromol. 297 (2025) 139896.
[5] B. Gatto, M. Palumbo, C. Sissi, Nucleic acid aptamers based on the G-quadruplex structure: therapeutic and diagnostic potential, Curr. Med. Chem. 16 (2009) 1248–1265.
[6] O.A. Alsaidan, Recent advancements in aptamers as promising nanotool for therapeutic and diagnostic applications, Anal. Biochem. 702 (2025) 115844.
[7] G. Santarpia, E. Carnes, Therapeutic Applications of Aptamers, Int. J. Mol. Sci. 25 (2024) 6742.
[8] M. Razlansari, S. Jafarinejad, A. Rahdar, M. Shirvaliloo, R. Arshad, S. Fathi-Karkan, S. Mirinejad, S. Sargazi, R. Sheervalilou, N. Ajalli, S. Pandey, Development and classification of RNA aptamers for therapeutic purposes: an updated review with emphasis on cancer, Mol. Cell. Biochem. 478 (2023) 1573–1598.
[9] A. Van den Avont, N. Sharma-Walia, Anti-nucleolin aptamer AS1411: an advancing therapeutic, Front. Mol. Biosci. 10 (2023) 1217769.
[10] C. Riccardi, E. Napolitano, C. Platella, D. Musumeci, M.A.B. Melone, D. Montesarchio, Anti-VEGF DNA-based aptamers in cancer therapeutics and diagnostics, Med. Res. Rev. 41 (2021) 464–506.
[11] V. Esposito, D. Benigno, I. Bello, E. Panza, M. Bucci, A. Virgilio, A. Galeone, Structural and Biological Features of G-Quadruplex Aptamers as Promising Inhibitors of the STAT3 Signaling Pathway, Int. J. Mol. Sci. 24 (2023) 9524.
[12] H. Yu, R. Jove, The STATs of cancer–new molecular targets come of age, Nat. Rev. Cancer 4 (2004) 97–105.
[13] D. Godugu, R. Chilamakuri, S. Agarwal, STAT3 axis in cancer and cancer stem cells: From oncogenesis to targeted therapies, Biochim. Biophys. Acta Rev. Cancer 1880 (2025) 189461.
[14] C. Seibel, S. Pudewell, P. Rafii, J. Ettich, H.T. Weitz, A. Lang, P. Petzsch, K. Kohrer, D.M. Floss, J. Scheller, Synthetic trimeric interleukin-6 receptor complexes with a STAT3 phosphorylation dominated activation profile, Cytokine 184 (2024) 156766.
[15] S.A. Jones, B.J. Jenkins, Recent insights into targeting the IL-6 cytokine family in inflammatory diseases and cancer, Nat. Rev. Immunol. 18 (2018) 773–789.
[16] M.A. Samad, I. Ahmad, A. Hasan, M.H. Alhashmi, A. Ayub, F.A. Al-Abbasi, A. Kumer, S. Tabrez, STAT3 signaling pathway in health and disease, MedComm 6 (2020) (2025) e70152.
[17] Y. Gu, I.S. Mohammad, Z. Liu, Overview of the STAT-3 signaling pathway in cancer and the development of specific inhibitors, Oncol. Lett. 19 (2020) 2585–2594.
[18] R.L. Carpenter, H.W. Lo, STAT3 Target Genes Relevant to Human Cancers, Cancers (Basel) 6 (2014) 897–925.
[19] J.K. Nagpal, R. Mishra, B.R. Das, Activation of Stat-3 as one of the early events in tobacco chewing-mediated oral carcinogenesis, Cancer 94 (2002) 2393–2400.
[20] J.L. Geiger, J.R. Grandis, J.E. Bauman, The STAT3 pathway as a therapeutic target in head and neck cancer: Barriers and innovations, Oral Oncol. 56 (2016) 84–92.
[21] P. Dutta, N. Sabri, J. Li, W.X. Li, Role of STAT3 in lung cancer, JAKSTAT 3 (2014) e999503.
[22] J.H. Ma, L. Qin, X. Li, Role of STAT3 signaling pathway in breast cancer, Cell Commun. Signal 18 (2020) 33.
[23] M. Tolomeo, A. Cascio, The Multifaced Role of STAT3 in Cancer and Its Implication for Anticancer Therapy, Int. J. Mol. Sci. 22 (2021) 603.
[24] J. Turkson, R. Jove, STAT proteins: novel molecular targets for cancer drug discovery, Oncogene 19 (2000) 6613–6626.
[25] D.E. Levy, G. Inghirami, STAT3: a multifaceted oncogene, Proc. Natl. Acad. Sci. USA 103 (2006) 10151–10152.
[26] Y. Hu, Z. Dong, K. Liu, Unraveling the complexity of STAT3 in cancer: molecular understanding and drug discovery, J. Exp. Clin. Cancer Res. 43 (2024) 23.
[27] A. Virgilio, A. Pecoraro, D. Benigno, A. Russo, G. Russo, V. Esposito, A. Galeone, Antiproliferative Effects of the Aptamer d(GGGT)(4) and Its Analogues with an Abasic-Site Mimic Loop on Different Cancer Cells, Int. J. Mol. Sci. 23 (2022) 5952.

[28] N.Q. Do, K.W. Lim, M.H. Teo, B. Heddi, A.T. Phan, Stacking of G-quadruplexes: NMR structure of a G-rich oligonucleotide with potential anti-HIV and anticancer activity, Nucleic Acids Res. 39 (2011) 9448–9457.
[29] V. Esposito, D. Benigno, C. Aliberti, C. Esposito, E. Panza, A. Virgilio, A. Galeone, Effects of 5-Methyl-2'-Deoxycytidine in G-Quadruplex Forming Aptamers d(G(3)C)(4) and d[GCG(2)(CG(3))(3)C]: Investigating the Key Role of the Loops, Biomolecules 15 (2025) 753.
[30] M. Sadrkhanloo, M.D.A. Paskeh, M. Hashemi, R. Raesi, M. Motahhary, S. Saghari, L. Sharifi, S. Bokaie, S. Mirzaei, M. Entezari, A.R. Aref, S. Salimimoghadam, M. Rashidi, A. Taheriazam, K. Hushmandi, STAT3 signaling in prostate cancer progression and therapy resistance: An oncogenic pathway with diverse functions, Biomed. Pharmacother. 158 (2023) 114168.
[31] P. Weerasinghe, Y. Li, Y. Guan, R. Zhang, D.J. Tweardy, N. Jing, T40214/PEI complex: a potent therapeutics for prostate cancer that targets STAT3 signaling, Prostate 68 (2008) 1430–1442.
[32] J. Zhou, J. Rossi, Aptamers as targeted therapeutics: current potential and challenges, Nat. Rev. Drug Discov. 16 (2017) 181–202.
[33] C. Yang, Y. Jiang, S.H. Hao, X.Y. Yan, F. Hong, H. Naranmandura, Aptamers: an emerging navigation tool of therapeutic agents for targeted cancer therapy, J. Mater. Chem. B 10 (2021) 20–33.
[34] S. Liu, X. Li, H. Gao, J. Chen, H. Jiang, Progress in Aptamer Research and Future Applications, ChemistryOpen 14 (2025) e202400463.
[35] M. Grau, E. Wagner, Strategies and mechanisms for endosomal escape of therapeutic nucleic acids, Curr. Opin. Chem. Biol. 81 (2024) 102506.
[36] D. Benigno, N. Navarro, A. Avino, V. Esposito, A. Galeone, A. Virgilio, C. Fabrega, R. Eritja, Aptamer-Drug conjugates for a targeted and synergistic anticancer Response: Exploiting T30923-5-fluoro-2'-deoxyuridine (INT-FdU) derivatives, Eur. J. Pharm. Biopharm. 201 (2024) 114354.
[37] G. Zhu, X. Chen, Aptamer-based targeted therapy, Adv. Drug Deliv. Rev. 134 (2018) 65–78.
[38] X. Tan, F. Jia, P. Wang, K. Zhang, Nucleic acid-based drug delivery strategies, J. Control. Release 323 (2020) 240–252.
[39] M. Liu, Y. Wang, Y. Zhang, D. Hu, L. Tang, B. Zhou, L. Yang, Landscape of small nucleic acid therapeutics: moving from the bench to the clinic as next-generation medicines, Signal Transduct. Target. Ther. 10 (2025) 73.
[40] H. Sun, Y. Zu, Aptamers and their applications in nanomedicine, Small 11 (2015) 2352–2364.
[41] M. Kim, D.M. Kim, K.S. Kim, W. Jung, D.E. Kim, Applications of Cancer Cell-Specific Aptamers in Targeted Delivery of Anticancer Therapeutic Agents, Molecules 23 (2018) 830.
[42] T. Gholikhani, S. Kumar, H. Valizadeh, S. Mahdinloo, K. Adibkia, P. Zakeri-Milani, M. Barzegar-Jalali, B. Jimenez, Advances in Aptamers-Based Applications in Breast Cancer: Drug Delivery, Therapeutics, and Diagnostics, Int. J. Mol. Sci. 23 (2022) 14475.
[43] Z. Fu, J. Xiang, Aptamer-Functionalized Nanoparticles in Targeted Delivery and Cancer Therapy, Int. J. Mol. Sci. 21 (2020) 9123.
[44] S. Fathi-Karkan, S. Mirinejad, F. Ulucan-Karnak, M. Mukhtar, H. Ghahramani Almanghadim, S. Sargazi, A. Rahdar, A.M. Diez-Pascual, Biomedical applications of aptamer-modified chitosan nanomaterials: An updated review, Int. J. Biol. Macromol. 238 (2023) 124103.
[45] A. Falanga, R. Bellavita, S. Braccia, S. Galdiero, Hydrophobicity: The door to drug delivery, J. Pept. Sci. 30 (2024) e3558.
[46] F. Davodabadi, S. Mirinejad, S. Fathi-Karkan, M. Majidpour, N. Ajalli, R. Sheervalilou, S. Sargazi, D. Rozmus, A. Rahdar, A.M. Diez-Pascual, Aptamer-functionalized quantum dots as theranostic nanotools against cancer and bacterial infections: A comprehensive overview of recent trends, Biotechnol. Prog. 39 (2023) e3366.
[47] F. Davodabadi, S. Mirinejad, S. Malik, A. Dhasmana, F. Ulucan-Karnak, S. Sargazi, S. Sargazi, S. Fathi-Karkan, A. Rahdar, Nanotherapeutic approaches for delivery of long non-coding RNAs: an updated review with emphasis on cancer, Nanoscale 16 (2024) 3881–3914.
[48] M. Yang, J. Li, P. Gu, X. Fan, The application of nanoparticles in cancer immunotherapy: Targeting tumor microenvironment, Bioact. Mater. 6 (2021) 1973–1987.
[49] R. Bellavita, S. Braccia, A. Falanga, S. Galdiero, An Overview of Supramolecular Platforms Boosting Drug Delivery, Bioinorg. Chem. Appl. 2023 (2023) 8608428.
[50] H. Cui, M.J. Webber, S.I. Stupp, Self-assembly of peptide amphiphiles: from molecules to nanostructures to biomaterials, Biopolymers 94 (2010) 1–18.
[51] J.D. Hartgerink, E. Beniash, S.I. Stupp, Self-assembly and mineralization of peptide-amphiphile nanofibers, Science 294 (2001) 1684–1688.
[52] K. Ozturk, M. Kaplan, S. Calis, Effects of nanoparticle size, shape, and zeta potential on drug delivery, Int. J. Pharm. 666 (2024) 124799.
[53] D. Kulkarni, S. Musale, P. Panzade, A.C. Paiva-Santos, P. Sonwane, M. Madibone, P. Choundhe, P. Giram, S. Cavalu, Surface Functionalization of Nanofibers: The Multifaceted Approach for Advanced Biomedical Applications, Nanomaterials (Basel). 12 (2022) 3899.
[54] R. Bellavita, M. Piccolo, L. Leone, M.G. Ferraro, P. Dardano, L. De Stefano, F. Nastri, C. Irace, A. Falanga, S. Galdiero, Tuning Peptide-Based Nanofibers for Achieving Selective Doxorubicin Delivery in Triple-Negative Breast Cancer, Int. J. Nanomedicine 19 (2024) 6057–6084.
[55] R. Bellavita, T. Barra, S. Braccia, M. Prisco, S. Valiante, A. Lombardi, L. Leone, J. Pisano, R. Esposito, F. Nastri, G. D'Errico, A. Falanga, S. Galdiero, Engineering Multifunctional Peptide-Decorated Nanofibers for Targeted Delivery of Temozolomide across the Blood-Brain Barrier, Mol. Pharm. 22 (2025) 1920–1938.
[56] V. Del Genio, A. Falanga, E. Allard-Vannier, K. Herve-Aubert, M. Leone, R. Bellavita, R. Uzbekov, I. Chourpa, S. Galdiero, Design and Validation of Nanofibers Made of Self-Assembled Peptides to Become Multifunctional Stimuli-Sensitive Nanovectors of Anticancer Drug Doxorubicin, Pharmaceutics 14 (2022) 1544.
[57] T. Barra, A. Falanga, R. Bellavita, V. Laforgia, M. Prisco, S. Galdiero, S. Valiante, gH625-liposomes deliver PACAP through a dynamic in vitro model of the blood-brain barrier, Front. Physiol. 13 (2022) 932099.
[58] S. Galdiero, A. Falanga, G. Morelli, M., Galdiero, gH625: a milestone in understanding the many roles of membranotropic peptides, Biochim. Biophys. Acta 1848 (1 Pt A) (2015) 16–25.
[59] H. Hossein-Nejad-Ariani, E. Althagafi, K. Kaur, Small Peptide Ligands for Targeting EGFR in Triple Negative Breast Cancer Cells, Sci. Rep. 9 (2019) 2723.
[60] C.N. Cultrara, S. Shah, G. Antuono, C.J. Heller, J.A. Ramos, U. Samuni, J. Zilberberg, D. Sabatino, Size Matters: Arginine-Derived Peptides Targeting the PSMA Receptor Can Efficiently Complex but Not Transfect siRNA, Mol. Ther. Nucleic. Acids. 18 (2019) 863–870.
[61] R. Bellavita, S. Braccia, M. Piccolo, P. Bialecki, M.G. Ferraro, S.F. Graziano, E. Esposito, F. Donadio, M. Bryszewska, C. Irace, E. Pedziwiatr-Werbicka, A. Falanga, S. Galdiero, Shielding siRNA by peptide-based nanofibers: An efficient approach for turning off EGFR gene in breast cancer, Int. J. Biol. Macromol. 292 (2025) 139219.
[62] R. Bellavita, E. Buommino, B. Casciaro, F. Merlino, F. Cappiello, N. Marigliano, A. Saviano, F. Maione, R. Santangelo, M.L. Mangoni, S. Galdiero, P. Grieco, A. Falanga, Synthetic Amphipathic beta-Sheet Temporin-Derived Peptide with Dual Antibacterial and Anti-Inflammatory Activities, Antibiotics (Basel). 11 (2022) 1285.
[63] A. Saviano, A.A. Manosour, F. Raucci, F. Merlino, N. Marigliano, A. Schettino, M. Wahid, J. Begum, A. Filer, J.E. Manning, G.M. Casillo, M. Piccolo, M.G. Ferraro, S. Marzano, P. Russomanno, R. Bellavita, C. Irace, J. Amato, M. Alfaifi, P. Rimmer, T. Iqbal, S. Pieretti, V. Vellecco, F. Caso, L. Costa, R. Giacomelli, R. Scarpa, G. Cirino, M. Bucci, H.M. McGettrick, P. Grieco, A.J. Iqbal, F. Maione, New biologic (Ab-IPL-IL-17) for IL-17-mediated diseases: identification of the bioactive sequence (nIL-17) for IL-17A/F function, Ann. Rheum. Dis. 82 (2023) 1415–1428.
[64] A. Ray, S. Das, N. Chattopadhyay, Aggregation of Nile Red in Water: Prevention through Encapsulation in beta-Cyclodextrin, ACS Omega 4 (2019) 15–24.
[65] R. Bellavita, A. Falanga, F. Merlino, G. D'Auria, N. Molfetta, A. Saviano, F. Maione, U. Galdiero, M.R. Catania, S. Galdiero, P. Grieco, E. Roscetto, L. Falcigno, E. Buommino, Unveiling the mechanism of action of acylated temporin L analogues against multidrug-resistant Candida albicans, J. Enzyme. Inhib. Med. Chem. 38 (2023) 36–50.
[66] M.G. Ferraro, F. Iazzetti, M. Bocchetti, C. Riccardi, D. Montesarchio, R. Santamaria, G. Misso, M. Piccolo, C. Irace, Ferroptosis Among the Antiproliferative Pathways Activated by a Lipophilic Ruthenium(III) Complex as a Candidate Drug for Triple-Negative Breast Cancer, Pharmaceutics 17 (2025) 918.
[67] M. Piccolo, C. Russo, V. Arciuolo, M.G. Ferraro, V. Abbate, A. Di Porzio, E. Cinquegrana, F.S. Di Leva, B. Pagano, A. Randazzo, R.C. Hider, C. Irace, J. Amato, M. Giustiniano, Design, Synthesis, and Anticancer Activity of Drug-like Iron Chelators/G-Quadruplex Binders as Synergic Dual Targeting Agents, J. Med. Chem. 68 (2025) 1245–1259.
[68] A. Renaud de la Faverie, A. Guedin, A. Bedrat, L.A. Yatsunyk, J.L. Mergny, Thioflavin T as a fluorescence light-up probe for G4 formation, Nucleic Acids Res. 42 (2014) e65.
[69] N.A. Hussein, S. Malla, M.A. Pasternak, D. Terrero, N.G. Brown, C.R. Ashby Jr., Y. G. Assaraf, Z.S. Chen, A.K. Tiwari, The role of endolysosomal trafficking in anticancer drug resistance, Drug Resist. Updat. 57 (2021) 100769.